Optimising lithium-ion cell design for plug-in hybrid and battery electric vehicles☆

Krishnakumar Gopalakrishnan[a,1,2], Ian D. Campbell[a,1,2,*], Monica Marinescu[a,3], Marcello Torchio[b], Gregory J. Offer[a,4], Davide Raimondo[c,5]

[a]*Department of Mechanical Engineering, Imperial College London, South Kensington, London SW7 2AZ, United Kingdom*
[b]*Dipartimento di Ingegneria Civile e Architettura, University of Pavia, 27100 Pavia, Italy*
[c]*Department of Electrical, Computer and Biomedical Engineering, University of Pavia, 27100 Pavia, Italy*

Abstract

Increased driving range and enhanced fast charging capabilities are two immediate goals of transport electrification. However, these are of competing nature, leading to increased energy and power demand respectively from the on-board battery pack. By fine-tuning the number of layers versus active electrode material of a lithium ion pouch cell, tailored designs targeting either of these goals can be obtained. Achieving this trade-off through iterative empirical testing of layer choices is expensive and often produces sub-optimal designs. This paper presents a model-based methodology for determining the optimal number of layers, maximising usable energy whilst satisfying specific acceleration and fast charging targets. The proposed methodology accounts for the critical need to avoid lithium plating during fast charging and searches for the optimal layer configuration considering a range of thermal conditions. A numerical implementation of a cell model using a hybrid finite volume-spectral scheme is presented, wherein the model equations are suitably reformulated to directly accept power inputs, facilitating rapid and accurate searching of the layer design space. We show how thermal management design can limit vehicle driving range at high charging temperatures. We highlight how electrode materials exhibiting increased solid phase diffusion rates are as equally important for extended range as developing new materials with higher inherent capacity. We illustrate for a plug-in hybrid vehicle, how the proposed methodology facilitates common module design of battery packs, thereby reducing the cost of derivative vehicle models. To facilitate model based layer optimisation, we provide the open-source toolbox, BOLD (Battery Optimal Layer Design).

Keywords: Li-ion battery, Pouch cell design, Layer optimisation, Pseudo-2D model, Electric vehicle, Fast charging

1. Introduction

Lithium-ion batteries are becoming an increasingly important part of modern day life, having become ubiquitous in portable electronic devices. The development of electric vehicles to tackle environmental challenges is driving an unprecedented demand for lithium-ion batteries. However, in automotive applications such as hybrid and electric vehicles, large-scale commercialisation has been hindered by the need for higher energy density cells at lower costs without compromising their power density [1]. Improvements are being sought through a multifaceted approach — i) through fundamental material advances [2, 3], ii) new chemistries [4], iii) novel cell designs and manufacturing techniques [5], iv) system design or reducing the costs of assembly [6, 7], and v) improved controller design for advanced battery management systems [8].

For accelerated product development, many industries have established a model-led approach, supplanting traditional strategies of iterative prototyping. The positive impacts brought about by this approach in the automotive industry have been discussed in [9, 10]. The salient benefits can be summed up as *a*) acceleration of design iterations and *b*) increased understanding gained from formalising empirical know-how. It has become inexpensive to explore design changes in a computer model, facilitating focussed lab development targeting high-yield improvements predicted through models. Furthermore, Becker *et al.* argue that a model-led approach subtly helps to develop fundamental understanding of underlying physical phenomena [10]. In the context of battery modelling, physics-based models can provide improved understanding of battery behaviour and a model-led approach can assist in accelerating the pace of battery development [11]. The use of reduced order electrochemical models [12]

☆Electronic Supplementary Information (ESI) available: See DOI: 10.5281/zenodo.1016406

*Corresponding author
Email addresses: krishnakumar@imperial.ac.uk (Krishnakumar Gopalakrishnan), i.campbell15@imperial.ac.uk (Ian D. Campbell), monica.marinescu@imperial.ac.uk (Monica Marinescu), marcello.torchio01@ateneopv.it (Marcello Torchio), gregory.offer@imperial.ac.uk (Gregory J. Offer), davide.raimondo@unipv.it (Davide Raimondo)

[1]These authors contributed equally to this work.
[2]Ph.D. Student, Dept. of Mechanical Engineering, Imperial College London
[3]Lecturer, Dept. of Mechanical Engineering, Imperial College London
[4]Sr. Lecturer, Dept. of Mechanical Engineering, Imperial College London, Fax: +44 20 7589 5111, Tel: +44 20 7594 7072
[5]Associate Professor, Department of Electrical, Computer and Biomedical Engineering, University of Pavia

as well as equivalent circuit models [13] for parameter estimation and control has become prevalent across a wide variety of battery applications. On the materials front, ab-initio modelling has been successfully employed to accelerate the development of new energy storage materials [14, 15]. Furthermore, large-scale computational screening has been used for identifying promising candidate materials for solid-state batteries [16].

However, the integration of full order electrochemical models of lithium-ion batteries into optimisation frameworks for cell design is still in an embryonic phase. The numerous complex physical phenomena (intercalation, diffusion, kinetics) of battery systems pose significant computational challenges to fast and efficient simulations required for such large-scale design simulations [17]. The vertical integration of such models across multiple length scales, albeit critical to increase their applicability for design engineers, is also rare. Despite its popularity in academia, the most-commonly cited Pseudo two-dimensional (P2D) model developed by Doyle, Fuller & Newman [18] has not seen industry-wide uptake, particularly in cell design applications. Industry-focussed tools such as Battery Design Studio (CD-adapco), Star-CCM+, ANSYS Fluent and COMSOL's Batteries & Fuel Cells Module have been used to solve *a*) design optimisation problems at the pack-level [19], *b*) optimise thermal management systems centered around an empirically-chosen cell design [20], and *c*) predict lithium plating [21]. However, the commercial nature of such packages poses a cost-barrier to the desirable transition from empirical to model-led design. Restricted access to details of model set-up and limited choice of numerical solvers further tend to disincentivise their widespread use. Open-source cell modelling tools such as DUALFOIL [22] and LIONSIMBA [23] equip users with full control and provide insight into detailed implementation of model equations within the software, and hence present feasible alternatives for rapid adoption.

In this work, we report a multi-scale design methodology, fully integrated from the vehicle's drivetrain level down to the cell's electrode level, for rapidly evaluating and screening hundreds of layer choices for cell designs against the most aggressive power requirements of an Electric Vehicle (EV) or Plug-in Hybrid Electric Vehicle (PHEV), *viz.* quick vehicular acceleration and fast charging whilst staying close to lithium-plating boundary. The resulting choice of layers represents the optimum number of elementary electrochemical layers to be stacked within a pouch cell of fixed exterior dimensions. Our work is analogous to computational screening of materials [16], wherein we efficiently screen pouch cell layer configurations at different initial and ambient temperature combinations for given load demands so as to maximise the All Electric Range (AER). In this work, we assume that *a*) the arrangement of cells within a pack module is given (fixed module design), and *b*) the exterior dimensions of the pouch cell is fixed. This scenario enables a vehicle manufacturer to adopt a common-module design across their entire xEV portfolio. The proposed methodology can be applied with minimal modification to optimally design pouch cells of current and future battery chemistries.

The paper is organised as follows. In Section 2, the concept of trade-off in usable energy versus power capability of a lithium-ion cell is discussed and their dependence on number of layers is demonstrated. Section 3.1 provides a description of the proposed methodology used to arrive at the optimal layer choice for a given set of design objectives. A key component of the BOLD toolbox is a variant of the open source cell simulation software, LIONSIMBA. The original version of this toolbox has been suitably modified to include specific capabilities that enable layer optimisation of pouch cells. Section 3.2 presents the mathematical reformulations and numerical implementation that facilitates the toolbox's usage for this layer optimisation study. Section 4 presents the results of applying the methodology presented in Section 3.1 to two vehicular platforms — a) Battery Electric Vehicle (BEV) and b) PHEV. A detailed analysis of the impact of acceleration and fast-charging specifications on the optimal layer choice is performed. Applicability of the procedure to a wide range of design circumstances is also discussed. Section 5 draws conclusions regarding the impact of this model-led layer optimisation methodology on future cell designs. Exploring the extent of validity of the inherent assumptions of this layer-optimisation framework, the paper ends with potential directions for further work that could accelerate adoption of model-based cell design in the community.

2. Optimal Layer Configuration

In a typical lithium-ion cell design, there exists a trade-off between its energy (capacity) and power-delivery capability (resistance). For an xEV with a given pack configuration, the AER is limited by the cell's capacity, while acceleration and fast charging represent the worst-case operational power demands. A design consideration necessitated by this phenomena is the choice of number of layers in a cell, with one layer consisting of i) positive current-collector, ii) positive electrode, iii) separator, iv) negative electrode, and v) negative current-collector. In this work, we consider a pouch cell with fixed exterior dimensions, such that the height of the electrochemical stack within the pouch is constant. Furthermore, the thickness of current collectors and separator material are also fixed. The case of more layers inside the cell corresponds to thinner electrodes and less active material (i.e. lower capacity). This, however results in larger electrode surface area per cell, as well as higher electrical and thermal conductivities due to the presence of more current collectors (i.e. higher power capability). Fewer units inside the cell correspond to the presence of more active material and therefore capacity. However, this results in lower surface area and hence reduced power capability. Thicker electrodes also lead to less homogenous reaction-rate distributions along the thickness of the electrodes [24].

This trade-off between the cell's energy and power upon varying the number of layers is illustrated in Fig. 1; these are model predictions for a galvanostatic discharge of a $LiCoO_2$/graphite cell with parameters given in table 2. During the first few minutes of discharge, the cell's terminal voltage is highest for the cells with the highest layer counts, *viz.* $n = \{90, 70\}$, having comparitively lower resistances. However, they contain a lower volume of active material leading to reduced capacity compared to $n = 50$. In contrast to this, with $n = 10$, the cell's terminal

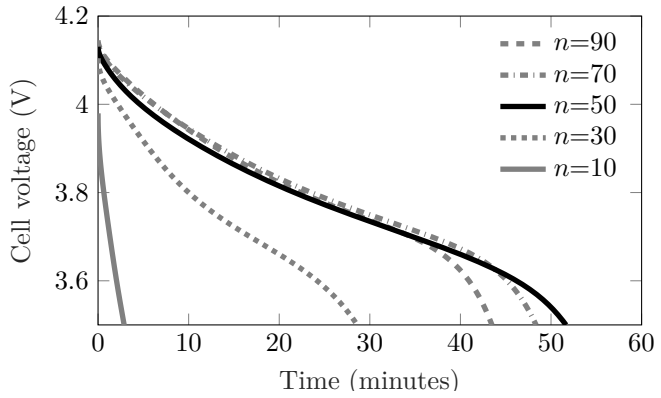

Figure 1 Terminal voltage curves of a Li-ion cell (with parameters given in table 2) under a 60 A galvanostatic discharge from 100% State of Charge (SOC) until lower cut-off voltage for a few layer choices, n, in a pouch cell of fixed exterior height. The maximum usable energy is achieved for an intermediate choice of n, that corresponds to neither the highest nominal capacity layer configuration (n=10) nor the highest electrode surface area configuration (n=90).

voltage collapses immediately and hits the voltage cut-off whilst the SOC is as high as 96 %. This is because the resistance of those cells with very few layers is significantly high, resulting in high overpotentials within the cell. Table 1 shows a comparison of the cell's usable energy under a galvanostatic discharge for a few layer choices. It highlights that, although the theoretical capacity Q_n of a cell may be high, the usable energy that can be extracted in an application is abysmal at very low layer counts.

Owing to the dependence of its nominal capacity on the number of layers n, the cell's C-rate does not remain constant during a galvanostatic discharge (refer table 1). Similarly, with constant power inputs, discussed in the remainder of this work, the ratio of power to nominal capacity — known as the E-rate — also does not remain constant when n varies. For the scenario discussed thus far, an intermediate choice of number of layers, e.g. $n = 50$, represents just one of many possible compromises between the surface area available for reaction and the total volume of active material. Among the finite layer configurations considered here, this layer choice offers the greatest usable energy at the chosen discharge rate. This is symptomatic of the (downward opening) parabolic relationship between a cell's usable energy and its number of layers.

Table 1 Theoretical capacity and usable energy of a Li-ion cell (with parameters given in table 2) upon varying the number of layers under a 60 A galvanostatic discharge

n	Q_{n} (Ah)	C-rate	Usable energy (Wh)	SOC (%)
90	48.25	1.24	166.20	10.0
70	53.99	1.11	184.40	10.5
50	59.73	1.00	195.39	13.6
30	65.47	0.92	107.93	56.2
10	71.21	0.84	10.67	96.0

Taking cognizance of this phenomenon, we propose a layer optimisation methodology in 3.1, whose scope within the hierarchical powertrain architecture of a typical xEV is shown in Fig. 2. The xEV powertrain may be decomposed into that for a BEV by omitting those components to the left of the battery pack. The assumed BEV powertrain thus consists of *a*) battery pack, *b*) three-phase inverter, *c*) Permanent Magnet Synchronous Motor (PMSM), *d*) gearbox for torque multiplication, and *e*) rest of the power train (differential shaft and driven wheels). When all components in the powertrain schematic (Fig. 2) are considerded, one obtains a series plug-in hybrid configuration. In this case, a downsized Internal Combustion Engine (ICE), coupled to the pack's DC bus through a generator and three-phase rectifier, can be used to supply a portion of the mechanical power, and/or to partially charge the battery during propulsion. All discharge simulations of the PHEV were conducted with the powertrain operating in all-electric mode, i.e. charge-depletion case, so that the cells are designed for the worst-case operating scenario, i.e. without assistive power from the ICE. For both xEV platforms, the source of applied battery pack power is either fast charging from the mains, $P_{\mathrm{batt}}^{\mathrm{fastchg}}$ (charge), or acceleration, $P_{\mathrm{batt}}^{\mathrm{acc}}$ (discharge) which is computed from the power required at the wheels, P_{w}. We employ the convention that positive powers represent charge, and negative powers, discharge respectively. The BEV pack configuration consists of 3 parallel strings of 8 series-connected modules. The PHEV pack consists of a single string of 8 series-connected modules. All pack modules are assumed to be identical across both xEV platforms. Usage of a single, identical module is feasible since they contain cells with fixed exterior geometry. The complete set of parameters of the pouch cells are given in table 2. Within any module, there are 12 series-connected identical cells — denoted by battery circuit symbols on the left side of Fig. 2. This architecture yields a 96S–3P cell configuration for the BEV battery. The PHEV pack has one-third the number of cells of the BEV pack, resulting in a 96S–1P configuration. However, since they consist of the same number of series cells, both packs provide the same DC bus voltage. By computing the power required at the pack's terminals, and assuming its even distribution across all the cells within the pack, a first-order design ballparking of the cell's layers can be made through simulation of just a single cell. In doing so, we make the simplifying (and simulation runtime reducing) assumption that the conditions of any one cell are representative of those of any other cell. Although this assumption shall most likely be violated in actual vehicle operation, modern advanced battery management systems actively strive to maintain such a state (SOC, Temperature etc.) through pack balancing and thermal management strategies, thereby justifying these assumptions by minimising the excursion of cell-to-cell deviations within a controlled envelope.

For a single xEV, each cell within a module consists of an identical number of layers, n, as illustrated in the centre-foreground of the cell schematic within Fig. 2. We consider a tab-cooled thermal management system for the cells — a strategy that has been demonstrated to provide i) an 8 percentage point increase in the usable capacity of pristine cells versus that

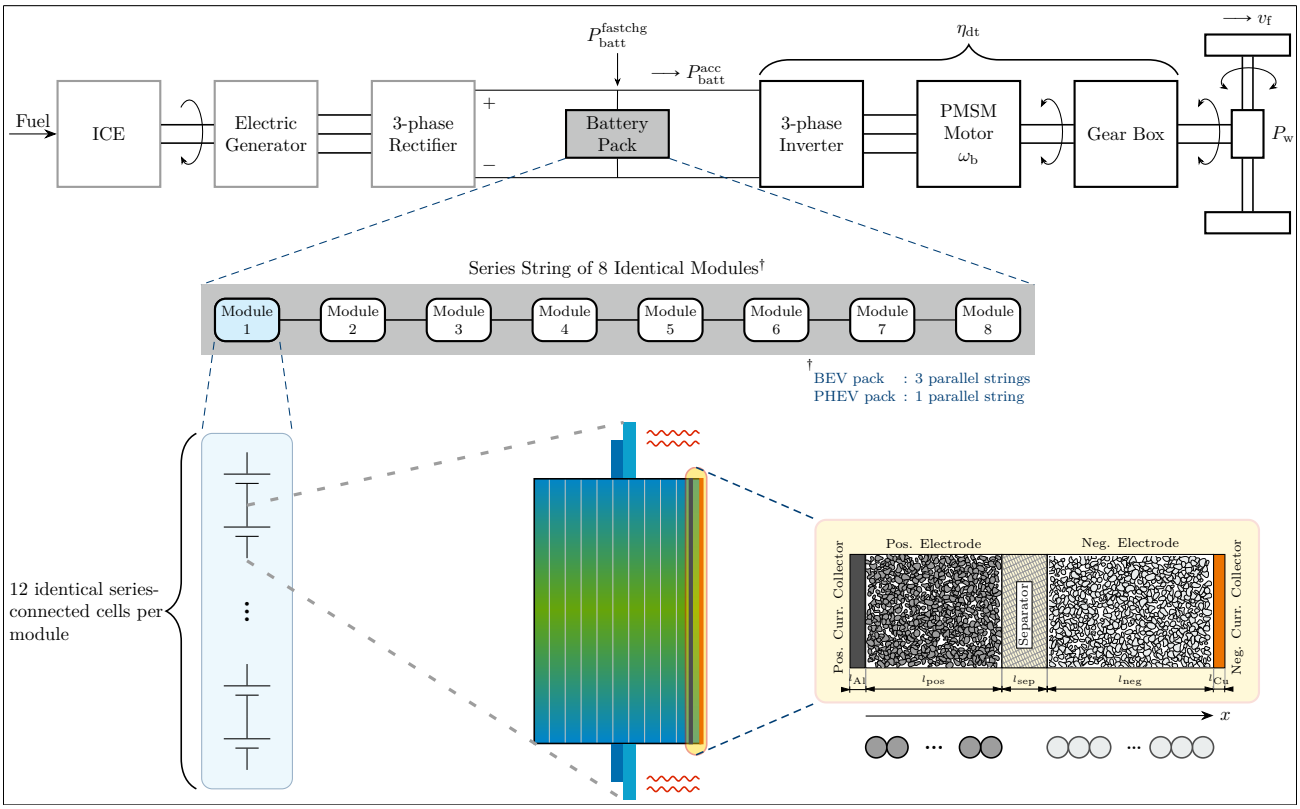

Figure 2 Schematic representing the vehicle–to–cell hierarchical overview of a typical electrified powertrain architecture. This represents the system-level context within which the proposed layer optimisation framework has been developed. Two xEV powertrains — a) BEV and b) series PHEV — are chosen as examples to demonstrate how the methodology facilitates common module designs for such battery packs.

achieved through surface cooling, and ii) as little as one-third the rate of loss of usable capacity over one thousand cycles — equivalent to a 3x extension of pack life [7]. The effect has been shown to be particularly prevalent at high powers, such as those experienced during xEV acceleration and fast charging. Tab cooling induces small thermal gradients within the plane of the layers, along the cell's longest axis and hence have negligible influence on its electrochemical performance. Since we assume there is no heat loss from the cell surfaces, no thermal gradients exist in the through-thickness direction, and all n layers along any 1D through-cell-thickness axis can be considered to be at the same temperature. In this scenario, a lumped thermal model of the cell is justified [25]. It is therefore possible to simulate only a one-dimensional, through-thickness segment of a single cell layer as depicted in the right foreground of Fig. 2. A suitably scaled version of the P2D model, representative of the overall cell, thereby completes the final link between the system-level demands at the vehicle's drivetrain to the electrochemical/thermal phenomena experienced at the electrodes. For both xEV platforms, a convective heat transfer coefficient, h (refer table 2), that is typical of forced air convection over cooling tabs (located at either end of the cell) is used [25]. T_{sink} denotes the temperature of the thermal sink, i.e. the coolant used in the thermal management system. For any given simulation, T_{sink} is held constant and the cell temperature $T_{\text{cell}}(t)$, which is bi-directionally coupled to the electrochemical model, evolves such that the rate of heat transfer between cell and coolant can vary. The lumped specific heat capacity of the cell is computed as a function of the cell's constituents as well as the layer configuration, as described in 3.1. Finally, the P2D model (reformulated to handle power inputs) in the right foreground of Fig. 2, is described in 3.2 and its underlying equations are given in AppendixA.

3. Optimisation Framework

3.1. Methodology

The methodology considers only the power requirements of acceleration and fast charging since they are significantly higher than any others encountered by the xEV pack. Thus, it would be superfluous to optimise layer configurations based upon drive cycle power profiles. This fact is quantitatively demonstrated in Section 4. Hence the methodology we present consists of two pathways — xEV acceleration and xEV fast charging. Fig. 3 is a schematic representation of the proposed layer optimisation methodology. We first consider the derivation of an optimal layer configuration via the acceleration pathway, using this schematic for support throughout.[1]

[1]The acceleration and fast charging pathways are independent of each other and can be traversed in parallel. However, in the BOLD toolbox the acceleration pathway is first considered, and the optimal layer configuration produced from it is used to narrow the search space for the fast charging pathway, providing a more refined, faster simulation overall.

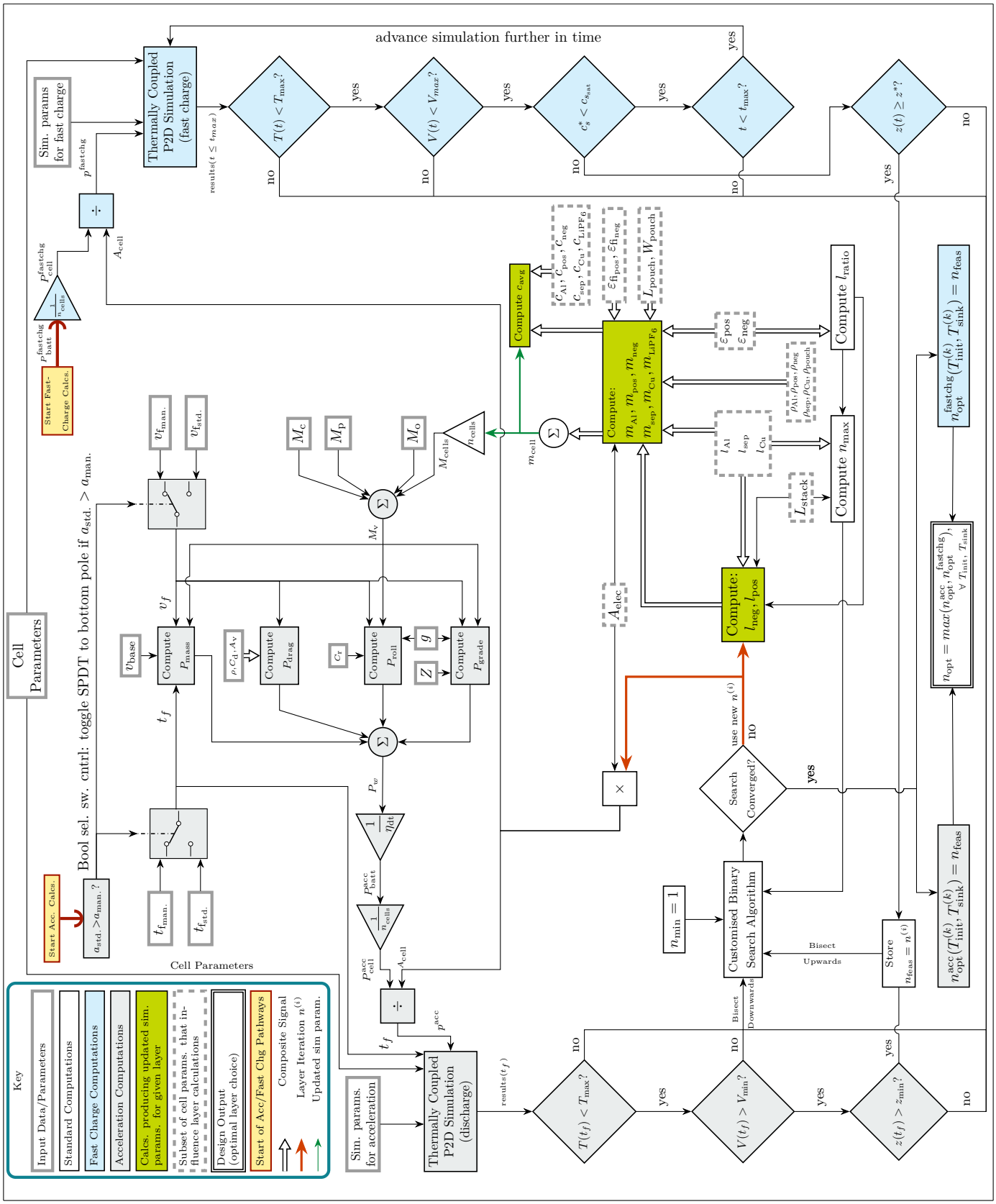

Figure 3 Flow diagram depicting an overview of the proposed layer optimisation methodology for Li-ion pouch cells.

Beginning at the acceleration pathway start point, "Start Acc. Calcs." (in yellow), in the left background of Fig. 3, a manufacturer-defined acceleration target, a_{man}, is evaluated against an acceleration target specified by the governing standards, $a_{\text{std.}}$. These are computed from the final speed, $v_{\text{f,man}}$ or $v_{\text{f,std.}}$, and target time within which to attain that speed, $t_{\text{f,man}}$ or $t_{\text{f,std.}}$, by accelerating from rest. The two Single Pole Double Throw (SPDT) Boolean switches indicate that only the values of v_{f} and t_{f} corresponding to the greater, i.e. more stringent, of the two acceleration targets are used further in calculations, and the others discarded, to facilitate design for the worst-case demand. The acceleration power required at the wheels, P_{w}, must be first computed in order to ultimately obtain the discharge power demanded from the pack, $P_{\text{batt}}^{\text{acc}}$. Following standard vehicle dynamics calculations, P_{w} is given by eqn (1).

$$P_{\text{w}} = P_{\text{mass}} + P_{\text{drag}} + P_{\text{roll}} + P_{\text{grade}} \tag{1}$$

$$P_{\text{mass}} = \frac{1}{2}\frac{M_{\text{v}}(n)}{t_{\text{a}}}\left(v_{\text{b}}^2 + v_{\text{f}}^2\right) \tag{1a}$$

$$P_{\text{drag}} = \frac{1}{2}\left(\rho_{\text{air}} C_{\text{d}} A_{\text{v}} v_{\text{f}}^3\right) \tag{1b}$$

$$P_{\text{roll}} = C_{\text{r}} M_{\text{v}}(n) g v_{\text{f}} \tag{1c}$$

$$P_{\text{grade}} = M_{\text{v}}(n) Z g v_{\text{f}} \tag{1d}$$

The terms constituting eqn (1) account for the power required to; accelerate the vehicle mass, P_{mass}, overcome air resistance, P_{drag}, overcome rolling resistance, P_{roll}, and negotiate a road gradient, P_{grade}. t_{a} and v_{f} are the acceleration time and final speed corresponding to the greater of $\{a_{\text{man}}, a_{\text{std}}\}$, obtained earlier, but with generic notation carried forward. v_{b} is the base speed of the xEV, corresponding to the highest speed at which its traction motor can provide maximum (rated) torque. All three terms are connected with arrows to the "Compute P_{mass}" block, indicating their use in computing P_{mass}. A few additional parameters — encased in solid grey boxes as the per the figure key in the left background of Fig. 3 — are required in computing the remaining power terms. g is the value of gravitational acceleration, and except $M_{\text{v}}(n)$, which we describe below, all other terms are also constants whose values are given in tables 3a and 3b. Summation of all power terms is indicated by the circular summation ($\sum$) block, resulting in P_{w}. $M_{\text{v}}(n)$ is a composite term for the xEV's mass and is dependent upon the pack mass, which in-turn depends upon the number of layers, n, in each cell. In the schematic, this is shown as output of the circular $\sum$ block in the centre of the schematic. This summation incorporates xEV chassis mass, M_{c}, the vehicle payload, M_{p}, pack overhead, M_{o}, and finally, the mass of all the cells within the pack, M_{cells}. The computation of M_{cells} is described later.

To compute the power demanded at the battery pack terminals, $P_{\text{batt}}^{\text{acc}}$, we scale the power required at the wheels by the drive train's efficiency, which is the product of its individual component efficiencies. Although in practice, these component efficiencies are functions of operating conditions such as inverter currents, vehicle speed, torque, wheel slip etc. for the sake of simplicity, we assume a constant lumped drive train efficiency, η_{dt}. The scaling process is depicted in Fig. 3 by the triangular gain block containing the inverse of η_{dt}, whose output is $P_{\text{batt}}^{\text{acc}}$. The pack power demand is then scaled down by the number of cells in the pack, n_{cells}, to arrive at the discharge power demanded of each cell, $P_{\text{cell}}^{\text{acc}}$. Since the P2D model equations are based upon normalised unit area and is applicable only to each electrochemical layer, we finally scale the per-cell discharge power by the electrochemically active surface area of a single cell, A_{cell}, to obtain p^{acc}. The overall surface area depends directly on the number of layers, which is the value being optimised for, as described in the text below.

For any given layer choice, its associated power density p^{acc}, and a given temperature combination $\{T_{\text{init}}, T_{\text{sink}}\}$, the P2D simulation ("Thermally Coupled P2D Simulation (discharge)", left centre), is initiated with a set of input acceleration parameters (tables 3a and 3b), a set of cell parameters (table 2) and a simulation end time, t_{f}. At the end of a simulation run, the outputs are evaluated at time t_{f} against user-settable values of maximum permissible cell temperature, T_{max}, minimum permissible cell voltage, V_{min}, and minimum permissible SOC, z_{min}, to determine whether the cell with the chosen layers can provide sufficient power to meet the acceleration power demand. These criteria are depicted in the three rhombi located in the left foreground of Fig. 3. If the cell fails to satisfy the power demand without exceeding the constraints (i.e. the output of any one of the three rhombi is false), that layer configuration's State of Function (SOF) is deemed to be zero and the search algorithm ("Customised Binary Search Algorithm", left foreground) is invoked again to choose a new layer configuration to be trialled. If the layer configuration succeeds in meeting the power demand (i.e. the output of the lowermost rhombus is true), that layer configuration's SOF is deemed to be unity, and that feasible value of n is assigned to n_{feas}. Two scenarios may then materialise; i) this value of n_{feas} is the lowest value of n that satisfies the power requirements or ii) a further lower value, of $n < n_{\text{feas}}$ still exists that can satisfy the power requirements. The termination of the search space bisection process embodied by the "Searched Converged?" rhombus (centre foreground) determines which of the two scenarios presently holds. For the former scenario, n_{feas} is then known to be the optimal (minimum) layer configuration satisfying the acceleration power requirements at this temperature combination, $n_{\text{opt}}^{\text{acc}}(T_{\text{init}}^{(\text{k})}, T_{\text{sink}}^{(\text{k})})$. For the latter scenario, n is varied according to the search algorithm in a continued effort to determine the lowest feasible layer count. Upon determination of $n_{\text{opt}}^{\text{acc}}$, the cell with the optimal layer configuration is subjected to continued discharge immediately following the end of xEV acceleration at time t_{f}. This represents the constant speed phase of the acceleration test criterion as defined in the Society of Automotive Engineers (SAE) standard J1666. During this phase, the xEV should have sufficient energy required to cover a distance of 1.609 k m (1 mile) at v_{f}. This is only included in the methodology for complete conformance with the standard and requires a relatively low amount of power that it has no influence on the determination of the optimal layer configuration for the acceleration run.

Fig. 3 indicates the usage of a bisection search algorithm

for the optimal layer count. However, the search algorithm, like the P2D model and the fast charging standard adopted, is yet another standalone component of this highly modular optimisation framework presented here. If so desired, this may be replaced with another variant by the user.[2]

Irrespective of the choice of search algorithm, when n is varied, a set of requisite parameter updates are applied to correctly represent the new layer configuration. Given the fixed available pouch height and the objective of maximising the energy stored within, a reduction in the number of layers mandates an increase in the thickness of both the negative and positive electrodes, l_{neg} and l_{pos}, respectively. Similarly, an increase in the number of layers mandates an electrode thickness reduction. Fig. 2 of Northrop et al. presents two possible topologies for stacking the layers within a pouch cell [26]. In one topology, the outermost current collectors of the stack are both copper. In the second topology, the outermost current collectors are composed of copper on one end and aluminium on the other. On the basis of these two possible topologies, we present the mathematical relationships between the thickness of the stack and that of the constituent domains. Although the stack topology wherein aluminium is placed at both ends is not considered in this work, the approach presented here can be trivially extended to this case.

L_{stack} is the available thickness within the pouch for the complete electrochemical stack. Its value is obtained by subtracting the thickness of two sheets of pouch material, T_{pouch}, — one upper and one lower — and two sheets of insulating separator of thickness l_{sep}, from the pouch height, H_{pouch}. Upper case L denotes the combined thickness of n number of a given component, while lower case l denotes the thickness of one unit of a component. The total thickness of all positive electrodes, negative electrodes, or separators, L_j, is the simple product of the number of layers and the thickness of any single unit of one of those components. It is given by eqn (2a). The total thickness of aluminium, L_{Al}, and of copper, L_{Cu}, current collectors is dependent upon whether the layer configuration is such that there exists an even or odd number of layers. These are given by eqn (2b) and (2c).

$$L_{\text{stack}} = \sum_j L_j(n) + L_{\text{Al}}(n) + L_{\text{Cu}}(n) \qquad \forall\, n \in \mathbb{N},\ j \in \{\text{pos, sep, neg}\} \tag{2}$$

$$L_j(n) = n l_j \tag{2a}$$

$$L_{\text{Al}}(n) = \begin{cases} \left(\frac{n}{2}\right) l_{\text{Al}}, & \text{if } n \text{ is even} \\ \left(\frac{n+1}{2}\right) l_{\text{Al}}, & \text{if } n \text{ is odd} \end{cases} \tag{2b}$$

$$L_{\text{Cu}}(n) = \begin{cases} \left(\frac{n+2}{2}\right) l_{\text{Cu}}, & \text{if } n \text{ is even} \\ \left(\frac{n+1}{2}\right) l_{\text{Cu}}, & \text{if } n \text{ is odd} \end{cases} \tag{2c}$$

[2] As an example of an alternative implementation, a linear search method, which iteratively goes through consecutive values of n in the ordered list between the minimum and maximum layer bounds, is also available in the BOLD toolbox. However, the computational complexity of this is $O(n)$, whereas the worst case convergence of the binary search algorithm is only logarithmic time, $O(\log n)$.

A key computation, *viz.* the recalculation of thickness of each individual electrode is represented by the green container in the centre foreground of Fig. 3, labelled "Compute: $l_{\text{neg}}, l_{\text{pos}}$", and is detailed in its entirety by eqns (3)–(5) derived through induction.

$$l_{\text{ce}} = \frac{L_{\text{stack}} - \lceil 0.5(n+1) \rceil l_{\text{cu}} - \lceil 0.5n \rceil l_{\text{al}}}{n} - l_{\text{sep}} \tag{3}$$

$$l_{\text{pos}} = \frac{l_{\text{ce}}}{l_{\text{ratio}} + 1} \tag{4}$$

$$l_{\text{neg}} = l_{\text{ce}} - l_{\text{pos}} \tag{5}$$

l_{ce} is the combined thickness of one positive and one negative electrode, computed using eqn (3). The l_{ratio} is given by eqn (9), described later, and enables computation of the individual electrode thickness values, as per eqn (4) and (5). It is these individual electrode thickness values that become the computational domain lengths in the P2D model simulations.

A second green container in the right foreground of Fig. 3 represents the updating of the cell mass as n varies. Cell mass is recomputed according to eqn (6) below, accounting for the changing total thickness of positive and negative electrode material, separator, and current collector materials. The mass of electrolyte, m_{LiPF_6}, and the mass of the pouch material, m_{pouch}, are however computed only once. m_{pouch} is independent of the choice of layer configuration, while we approximate m_{LiPF_6} as so. The circular $\sum$ block immediately above the green container in Fig. 3 represents the summation of the component masses. The cell mass m_{cell} is scaled by the overall number of cells within the pack to obtain the mass of all cells, M_{cells}, and forms a component of the vehicle's mass calculations.

$$m_{\text{cell}} = \sum_j m_j + m_{\text{Al}} + m_{\text{Cu}} + m_{\text{LiPF}_6} + m_{\text{pouch}},\ j \in \{\text{pos, sep, neg}\} \tag{6}$$

$$m_j = A_{\text{elec}} L_j \varepsilon_j \rho_j \tag{6a}$$

$$m_{\text{Al}} = A_{\text{elec}} L_{\text{Al}} \rho_{\text{Al}} \tag{6b}$$

$$m_{\text{Cu}} = A_{\text{elec}} L_{\text{Cu}} \rho_{\text{Cu}} \tag{6c}$$

$$m_{\text{LiPF}_6} = A_{\text{elec}} \left(\sum_j L_j (1 - \varepsilon_{\text{fi}_j} - \varepsilon_j) \right) \rho_{\text{LiPF}_6} \tag{6d}$$

$$m_{\text{pouch}} = 2 H_{\text{pouch}} L_{\text{pouch}} W_{\text{pouch}} \rho_{\text{pouch}} \tag{6e}$$

A third green container (right centre of Fig. 3) represents the updating of cell-averaged specific (gravimetric) heat capacity as n varies. Eqn (7) presents the associated calculations, wherein only the first three terms of the summation are dependent upon n. The latter two terms, associated with the pouch and electrolyte are independent of n. The heat capacities of any additive materials to electrodes, such as fillers and binders, are assumed to be negligible.

$$c_{\text{avg}} = \frac{1}{m_{\text{cell}}}\left[\sum_j c_j m_j + c_{\text{Al}} m_{\text{Al}} + c_{\text{Cu}} m_{\text{Cu}} + c_{\text{LiPF}_6} m_{\text{LiPF}_6} + c_{\text{pouch}} m_{\text{pouch}}\right], \qquad j \in \{\text{pos, sep, neg}\} \quad (7)$$

A central concept of this scheme is that, whilst recomputing all the above parameters, the ratio of negative to positive electrode thickness remains fixed. The computation of this ratio relies upon the key idea of electrode balancing, i.e. equating the volumes of active material constituting each electrode, as per eqn (8). This is represented in a standard computation container in the right foreground of Fig. 3, labelled "Compute l_{ratio}". Neglecting anode overhangs (< 2mm typical overhang to avoid edge plating), both electrode materials have the same planar area (overlap region). The difficulties in precisely manufacturing electrodes with porosities exactly matching prior design optimisation values are well recognised [27]. Hence, from a design perspective, porosity adjustments are not considered as attractive a choice as reconfiguring layers, in order to meet the energy versus power trade-offs. Consequently, we fix the electrode volume fractions in all design simulations (refer table 2). For the interested reader, a model-based investigation of usable capacity maximisation via electrode porosity variation is discussed in [28]. Considering equal surface areas and based on the above treatment of porosities, the ratio of electrode thickness is thus determined from the ratio of volume fractions in eqn (9).

$$A_{\text{elec}} l_{\text{neg}} \varepsilon_{\text{neg}} = A_{\text{elec}} l_{\text{pos}} \varepsilon_{\text{pos}} \quad (8)$$

$$l_{\text{ratio}} = \frac{l_{\text{neg}}}{l_{\text{pos}}} = \frac{\varepsilon_{\text{pos}}}{\varepsilon_{\text{neg}}} \quad (9)$$

The maximum number of layers that can be physically accommodated within L_{stack}, can be used as the initial upper bound for the search algorithm. This computation, labelled "Compute $n_{\max}$" is shown in the right foreground of Fig. 3. This computation can be expressed as a trivial mixed-integer optimisation task as shown in eqn (10). The objective function is to maximise the value of n subject to the physical constraint that the thickness of negative and positives electrodes remains positive.

$$\begin{aligned} \underset{n \in \mathbb{N}}{\max} \quad & n \quad (10)\\ \text{s.t.} \quad & l_{\text{pos}} = \left(\frac{L_{\text{stack}} - L_{\text{Al}}(n) - L_{\text{Cu}}(n) - n l_{\text{sep}}}{n(1 + l_{\text{ratio}})}\right) > 0 \\ & l_{\text{neg}} = \left(\frac{l_{\text{ratio}}(L_{\text{stack}} - L_{\text{Al}}(n) - L_{\text{Cu}}(n) - n l_{\text{sep}})}{n(1 + l_{\text{ratio}})}\right) > 0 \end{aligned}$$

Eqn (11) provides an analytical closed-form solution to the optimisation task posed in eqn (10). The two arguments of eqn (11) represent the maximum physically feasible number of even and odd layers respectively. $n_{\max}$ is taken as the larger of these two possibilities.

$$n_{\max} = \max\left(\left\lfloor \frac{2\,(L_{\text{stack}} - l_{\text{Cu}})}{l_{\text{Al}} + l_{\text{Cu}} + 2l_{\text{sep}}} \right\rfloor, \left\lfloor \frac{2L_{\text{stack}} - l_{\text{Al}} - l_{\text{Cu}}}{l_{\text{Al}} + l_{\text{Cu}} + 2l_{\text{sep}}} \right\rfloor\right) \quad (11)$$

The initial lower bound on the search space, $n_{\min}$, is a user input and is shown in the left foreground of Fig. 3. Its value may be chosen to be the physical minimum — one layer — as represented in Fig. 3. Alternatively, the lower bound may be set to an empirical value chosen by cell designers.

The fast charging pathway in Fig. 3, begins at the start point labelled "Start Fast-Charge Calcs." (yellow background box). The charging algorithm implemented here is a modified form of the one proposed in [29]. Being a modular framework, this may be replaced by another fast charging strategy if so desired. Our implementation differs from that presented in [29] in the following manner. Firstly, we replace the galvanostatic phase in [29] with a constant power phase. The battery pack charging power, $P_{\text{batt}}^{\text{fastchg}}$, is scaled down by the overall number of cells to obtain the per-cell charging power, $P_{\text{cell}}^{\text{fastchg}}$. This is shown by a gain block in the right background of Fig. 3. Power density, p^{fastchg}, is then computed by dividing by the overall electrode surface area A_{cell}. The P2D model is now invoked and while the simulation runs, the cell's state is continuously evaluated against various termination criteria (represented by five rhombi in the right background–foreground of Fig. 3)[3]. Cell temperature, $T(t)$ is constrained to remain below the maximum permissible value, $T_{\max}$. Similarly, the cell voltage must stay below the upper cut-off voltage, $V_{\max}$. If the molar concentration of lithium at the surface of negative electrode particles, c_{s}^*, reaches the saturation concentration, $c_{\text{s,sat}}$, the cell's SOC is evaluated against the end-of-charge SOC target, z^*. If $z(t) > z^*$, then the present layer choice represents the minimum (and hence optimal) value that can be used to charge to the desired target without lithium plating. Since the optimal layer configuration, $n_{\text{opt}}^{\text{fastchg}}$, is identified when the cell with the trialled layer configuration passes all the above-described criteria, it is deemed unnecessary to continue the charging process beyond the attainment of surface saturation. We therefore omit the pulsing phase of the charging algorithm in the interest of rapid traversal of the search space. This is the second major deviation of our implementation from that proposed in [29]. If $z(t) < z^*$ when $c_{\text{s}}^* = c_{\text{s,sat}}$, it implies that the cell with the present value of n cannot be charged sufficiently without succumbing to plating, and the search algorithm is called upon to provide a new layer configuration to trial. If however $c_{\text{s}}^* < c_{\text{s,sat}}\ \forall\, t$, then the charge time is evaluated against the upper limit for fast charge specifications, $t_{\max}$. If the time limit has not been reached, then the simulation marches forwards in time, and continues with the criteria evaluation process described above.

Both acceleration and fast charging pathways are traversed for various combinations of coolant and initial cell temperatures, (T_{init}, T_{sink}). Hence, in the space spanning the left to right foreground of Fig. 3, in the design output container, the optimal layer choice, n_{opt}, for each temperature combination is determined as

[3] Although Fig. 3 depicts the five criteria as being sequentially evaluated, the BOLD toolbox implements all of them simultaneously.

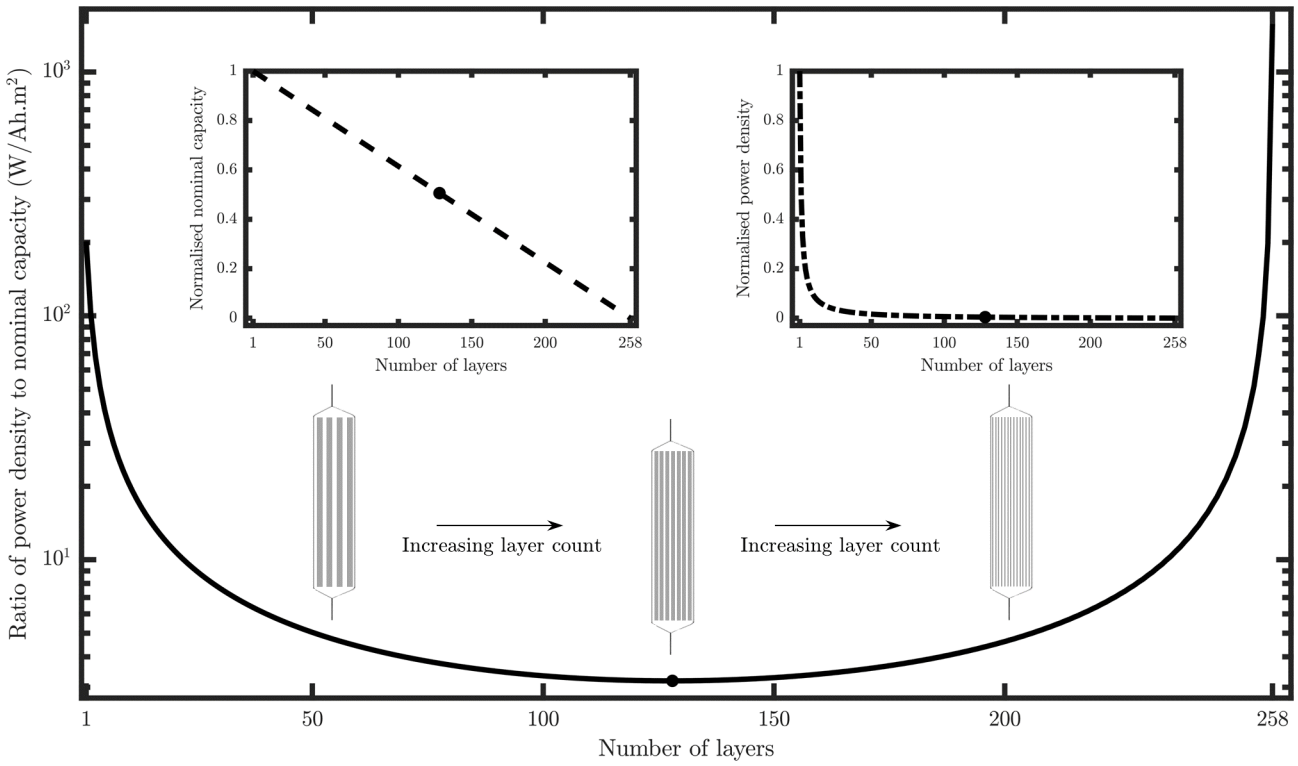

Figure 4 The ratio of power density to nominal cell capacity initially decreases monotonically reaching a minimum at $(n_{\max}/2 - n_{\min})$ layers. Left inset: Nominal capacity decreases linearly with n throughout the range $n_{\min} \leq n \leq n_{\max}$. Right inset: Power density declines rapidly for the first few layer choices and thereafter stabilises to a slow decay. It is desirable to design cells in the stable linear region of n to provide reliable error covariance bounds for online State of Available Power (SOAP) estimation algorithms.

the maximum of $(n_{\text{opt}}^{\text{acc}}, n_{\text{opt}}^{\text{fastchg}})$. Hence, the battery pack containing cells with n_{opt} layers is assured to meet both acceleration and fast charging demands. Extending upon the introduction to energy and power trade-off described in Sec 2, Fig. 4 illustrates the effect of varying the number of layers for constant power scenarios. Normalised nominal cell capacity decreases linearly with more rate capable layer configurations (upper left inset), while for a given applied power, normalised power density (upper right inset) decreases reciprocally. The curve (represented by solid line) in the main figure indicates how the ratio of power density to nominal capacity varies with n. The single black dot on each of the three curves represents the layer count, $n = n_{\text{ed}}$, at which this ratio is minimised. This layer count is given by $(n_{\max}/2) - n_{\min}$. For the 10×10^{-3} m tall cell pouch (whose maximum physically feasible layer count was determined to be 258 layers as per eqn 11), n_{ed} is computed to be 128 layers. The implication of the relation between declining nominal capacity and power density is that, for layer configurations to the left of the minimum point, there are large gains in available rate capability per reduction in energy density. For $n > n_{\text{ed}}$, it becomes increasingly expensive in terms of the energy density that must be sacrificed to gain each additional unit of rate capability. Hence, cells designed with layer configurations to the right of the minimum point n_{ed} make less efficient use of their available volume. Although such layer choices provide an equivalent ratio of power density to nominal capacity, they are less desirable than those to the left of n_{ed}. Nonetheless, depending on the harshness of fast charging and acceleration specifications, especially if pouch geometry is fixed, cell operation in the region of $n > n_{\text{ed}}$ may be deemed necessary, since despite their lower efficiency, they do provide marginal gains in absolute rate capability.

3.2. Electrochemical Model

The thermally-coupled, P2D electrochemical cell model used for simulating one layer is implemented in MATLAB [30], using a heavily-modified version of the LIONSIMBA toolbox [23]. The LIONSIMBA toolbox has already been validated against the results of DUALFOIL codes (which can be considered as the present benchmark standard). We have chosen LIONSIMBA here owing to its implementation in MATLAB with which the authors are more familiar. The simulation speeds using LIONSIMBA have been shown to be comparable to the FORTRAN implementation of DUALFOIL, primarily owing to its analytical Jacobian computation using automatic differentiation. For the full set of model equations, please refer to AppendixA. The parameter set used for simulation of this model is presented in table 2. Salient modifications to the toolbox that enable its use in the layer optimisation framework presented in Section 3 are given in 3.2.1 and 3.2.2.

3.2.1. Innate Power Input

The equations describing vehicle dynamics for acceleration are naturally formulated in terms of power demand, as per eqn (1).

Table 2 Cell and simulation parameters $j \in \{\text{Al, pos, sep, neg, Cu, LiPF}_6\text{, pouch}\}$

System

Parameter		Parameter	
Lower cutoff cell voltage, $V_{\min}$ (V)	[a] 3.50	Target cell SOC for fast charge, z^* (%)	[d] 80.00
Upper cutoff cell voltage, $V_{\max}$ (V)	[c] 4.20	Upper cell temperature limit, $T_{\max}$ (°C)	[e] 55.00

Geometric

Parameter	
Surface area of pos. & neg. electrode overlap within a layer, A_{elec} (m^2)	[b] 4.19×10^{-2}
Exterior pouch length, L_{pouch} (m)	[f] 332.74×10^{-3}
Exterior pouch width, W_{pouch} (m)	[f] 99.06×10^{-3}
Exterior pouch height, H_{pouch} (m)	[g] 10.00×10^{-3}
Pouch material thickness, T_{pouch} (m)	[h] 160.00×10^{-6}

Thermal

Parameter	Al CC	Pos	Sep	Neg	Cu CC	LiPF_6	Pouch
Specific heat capacity, c_j ($\text{J kg}^{-1}\text{ K}^{-1}$)	[i] 903.0	[i] 1269.2	[i] 1978.2	[i] 1437.4	[i] 385.0	[j] 133.9	[k] 1464.8
Density, ρ_j (kg m^{-3})	[l] 2700.0	[m] 2291.6	[b] 1100.0	[n] 2660.0	[l] 8960.0	[n] 1290.0	[o] 1150.0
Activation energy, diff. $E_{\text{act,s}_j}$ (J mol^{-1})	—	[p] 5000	—	[p] 5000	—	—	—
Activation energy, rxn. $E_{\text{act,k}_j}$ (J mol^{-1})	—	[p] 5000	—	[p] 5000	—	—	—
Heat transfer coefficient, h ($\text{W m}^{-2}\text{ K}^{-1}$)				[b] 150			
Total cell tab area, A_{tabs} (m^2)				[b] 5.94×10^{-3}			

Electrochemical

Parameter	Al CC	Pos	Sep	Neg	Cu CC
Thickness, l_j (m)	[g] 15×10^{-6}	eqn (4)	[p] 25×10^{-6}	eqn (5)	[p] 10×10^{-6}
Particle radius, R_{p_j} (m)	—	[p] 2×10^{-6}	—	[p] 2×10^{-6}	—
Material vol. fraction, ε_j	—	[p] 0.590	[p] 0.276	[p] 0.482	—
Filler vol. fraction, $\varepsilon_{\text{fi}_j}$	—	[p] 0.025	[p] 0	[p] 0.033	—
Bruggeman coefficient, brugg_j	—	[p] 4.00	[p] 4.00	[p] 4.00	—
Specific interfacial surface area, a_{s_j} ($\text{m}^2\text{ m}^{-3}$)	—	[p] 885×10^3	—	[p] 723.6×10^3	—
Electrolyte diffusivity, D_j ($\text{m}^2\text{ s}^{-1}$)	—	eqn (A.12)	eqn (A.12)	eqn (A.12)	—
Electrolyte conductivity, κ_j (S m^{-1})	—	eqn (A.14)	eqn (A.14)	eqn (A.14)	—
Electrode diffusivity, D_{s_j} ($\text{m}^2\text{ s}^{-1}$)	—	[p] 1×10^{-14}	—	[p] 3.9×10^{-14}	—
Electronic conductivity, σ_j (S m^{-1})	[p] 3.55×10^7	[p] 100.00	—	[p] 100.00	[p] 5.96×10^7
Stoichiometry, 0% SOC, $\theta_{\min_j}$	—	[q] 0.9917	—	[q] 0.0143	—
Stoichiometry, 100% SOC, $\theta_{\max_j}$	—	[r] 0.4955	—	[r] 0.8551	—
Max concentration, $c_{\text{s,max}_j}$ (mol m^{-3})	—	[p] 51 554	—	[p] 30 555	—
Saturation concen., $c_{\text{s,sat}}$ (mol m^{-3})	—	—	—	[s] 26 127.58	—
Reaction rate constant, k_{r_j} ($\text{m}^{2.5}\text{mol}^{-0.5}\text{s}^{-1}$)	—	[p] 2.33×10^{-11}	—	[p] 5.03×10^{-11}	—
Li^+ transference number, t_+^0	—	[p] 0.364	[p] 0.364	[p] 0.364	—
Init. electrolyte conc., $c_{\text{e},0}$ (mol m^{-3})	—	[p] 1000	[p] 1000	[p] 1000	—
Open circuit potential, U_j (V)	—	eqn (A.7)	—	eqn (A.8)	—
Faraday constant, F (C mol^{-1})			96 487		
Universal gas constant, R ($\text{J mol}^{-1}\text{ K}^{-1}$)			8.314		

Discretisation

Parameter	Pos	Sep	Neg
Nodes, through-thickness (axial), N_{a_j}	40	40	40
Nodes, within spherical particle (radial), N_{r_j}	15	—	15

[a] Calculated, as described in section 4 [b] Assumed [c] Ref.[31] [d] Ref.[32] [e] Ref.[8, 33] [f] Ref.[34] [g] Ref.[35] [h] Ref.[36]
[i] Ref.[37] [j] Ref.[38] [k] Computed based on the values of constituents in Ref.[39] [l] Ref.[39] [m] Ref.[40] [n] Ref.[41]
[o] Ref.[42] [p] Ref.[26] [q] Obtained via C/500 simulated discharge to 2.7 V [r] Ref.[43] [s] c_{s} at $z = 100$ %

Similarly, for fast charging, the power electronics components in all grid chargers have a finite maximum power delivery rating. It is desirable for an xEV battery pack to fully utilise the installed power capability of charging stations, and hence operate with a constant power input. Thus, there is a strong motivation to develop the P2D model equations to be amenable to accepting bi-directional power input. Attempts have been made in the literature to incorporate power input for lithium-ion battery simulation; e.g. Plett [44] provides a suitable methodology for equivalent circuit models. This involves the conversion of an input power, P_k, to a current, I_k, using an equivalent series resistance, R_0, which is updated at every fixed time index, k, as per eqn (12). v_k is the cell terminal voltage at the present time step, evolved from the applied current up to the prior time step.

$$I_k = \frac{v_k - \sqrt{v_k^2 - 4R_0P_k}}{2R_0} \tag{12}$$

There are two issues with such an approach. Firstly, application of this method to a P2D model requires an estimate of cell series resistance, which is incongruous with the philosophy of using a physics-based model. Secondly, eqn (12) is updated only at fixed multiples of the sample interval. A restriction to fixed time steps would render the methodology presented in Section 3 impractical because of the prohibitively long simulation times required to explore a search space of possible layer configurations, especially considering iterations over all thermal scenarios. Dees *et al.* recognised the requirement for a P2D model directly driven by applied power [45]. Furthermore, the simulation code DUALFOIL (since version 5.0) provides the option to accept power inputs [22]. However, the equations required to implement this specific case (such as changes to boundary conditions) have not been discussed in the literature. Hence, we provide here a brief derivation of the innate power density implementation.

Eqn (13) represents the standard solid phase potential Partial Differential Equation (PDE) of the P2D model. Eqns (13a) and (13b) represent the boundary conditions applied to eqn (13), where current density, i is the model input.

$$\frac{\partial}{\partial x}\left(\sigma_{\text{eff}}\frac{\partial \phi_{\text{s}}(x,t)}{\partial x}\right) = a_{\text{s}}Fj(x,t) \tag{13}$$

$$\sigma_{\text{eff}}\frac{\partial \phi_{\text{s}}(x,t)}{\partial x}\bigg|_{\substack{x=x_{\text{pos/Alcc}}\\ x=x_{\text{neg/Cucc}}}} = -\,i \tag{13a}$$

$$\sigma_{\text{eff}}\frac{\partial \phi_{\text{s}}(x,t)}{\partial x}\bigg|_{\substack{x=x_{\text{pos/sep}}\\ x=x_{\text{neg/sep}}}} = 0 \tag{13b}$$

To enable the model to be driven by applied power density p, we first replace the boundary condition in eqn (13a) with eqn (14), whilst satisfying the algebraic constraints (15) and (16), that arise from governing physical laws. Next, these equations, presented in continuous form, need to be suitably discretised for numerical implementation.

$$\sigma_{\text{eff}_{\text{neg}}}\left(\phi(x,t)\frac{\partial \phi_{\text{s}}(x,t)}{\partial x}\right)_{x=x_{\text{neg/Cucc}}} - \sigma_{\text{eff}_{\text{pos}}}\left(\phi(x,t)\frac{\partial \phi_{\text{s}}(x,t)}{\partial x}\right)_{x=x_{\text{pos/Alcc}}} = p \tag{14}$$

$$vi - p = 0 \tag{15}$$

$$v > 0 \tag{16}$$

The schematic in Fig. 5 shows the support mesh of a cell-centered FV discretisation scheme with uniformly-spaced nodes. Computational nodes are represented by dots, whereas the diffusion faces of control volumes are represented by vertical lines.

The weak form of eqn (13), applied on each control volume of the FV mesh, is given by eqn (17). Subscript k and $k \pm \frac{1}{2}$ denote the kth FV node and its associated faces respectively.

$$\sigma_{\text{eff}}\frac{\partial \phi_{\text{s}}(x,t)}{\partial x}\bigg|_{x_{k-\frac{1}{2}}}^{x_{k+\frac{1}{2}}} = a_{\text{s}}Fj_k(t)\,\Delta x \tag{17}$$

Applying boundary condition (13a) to the first and last control volumes of the positive and negative electrodes respectively, we obtain

$$\frac{-\sigma_{\text{eff}_{\text{pos}}}\phi_{\text{s}_0}}{\Delta x_{\text{pos}}} + \frac{\sigma_{\text{eff}_{\text{pos}}}\phi_{\text{s}_1}}{\Delta x_{\text{pos}}} + i = a_{\text{s}_{\text{pos}}}Fj_0\,\Delta x_{\text{pos}} \tag{18}$$

$$\frac{-\sigma_{\text{eff}_{\text{neg}}}\phi_{\text{s}_n}}{\Delta x_{\text{neg}}} + \frac{\sigma_{\text{eff}_{\text{neg}}}\phi_{\text{s}_{n-1}}}{\Delta x_{\text{neg}}} - i = a_{\text{s}_{\text{neg}}}Fj_n\,\Delta x_{\text{neg}} \tag{19}$$

The use of ϕ_{s_0} and ϕ_{s_n} in eqns (18) and (19) makes the approximation that the potentials at the centres of the outermost control volumes are equal to that at their corresponding current-collector interfaces. This simplification helps to maintain tractability of the mathematical reformulations. Slightly increased fidelity can be obtained by estimating the potentials at the interfaces, e.g. through extrapolation from two nearest FV node values, but at the cost of greatly increased boundary condition complexity. Multiplying eqn (18) with ϕ_{s_0}, eqn (19) by ϕ_{s_n} and subtracting the two resulting expressions yields the requisite boundary condition (eqn 20) for the solid phase potential PDE that may be applied to either electrode to enable application of

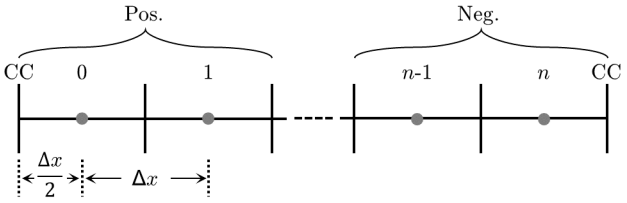

Figure 5 Schematic of a Finite Volume (FV) discretisation mesh, depicting nodes $0,\ 1,\ \ldots\ n-1, n$. The electrode–current collector interfaces are labelled 'CC'.

an input power density to the P2D model[4].

$$\frac{-\sigma_{\text{eff}_{\text{pos}}}\phi_{\text{s}_0}^2}{\Delta x_{\text{pos}}} - \frac{\sigma_{\text{eff}_{\text{neg}}}\phi_{\text{s}_n}^2}{\Delta x_{\text{neg}}} + \frac{\sigma_{\text{eff}_{\text{pos}}}\phi_{\text{s}_0}\phi_{\text{s}_1}}{\Delta x_{\text{pos}}} + \frac{\sigma_{\text{eff}_{\text{neg}}}\phi_{\text{s}_n}\phi_{\text{s}_{n-1}}}{\Delta x_{\text{neg}}} + p - a_{\text{s}_{\text{pos}}} F j_0 x_{\text{pos}} \phi_{\text{s}_0} - a_{\text{s}_{\text{neg}}} F j_n x_{\text{neg}} \phi_{\text{s}_n} = 0 \quad (20)$$

Eqn (20) being a quadratic, there exist two possible solutions for the solid phase potential. To obtain the unique physical solution, we impose the positivity constraint on the cell terminal voltage as per eqn (16), whose discretised form is given by eqn (21). The computation of the layer current density, i is aided by eqn (15), the discretised form of which is given by eqn (22). In this case, the potentials at each current collector interface is computed obtained via linear extrapolation from the two nearest FV cell centres. The DAE solver IDA [46], employed by LIONSIMBA toolbox facilitates handling of these additional algebraic constraints. Fig. 6 illustrates an example simulation demonstrating the capability to apply power inputs to the P2D model.

$$\phi_{s_p} - \phi_{s_n} > 0 \quad (21)$$

$$0 = i - \frac{p}{1.5\phi_{\text{s}_0} - 0.5\phi_{\text{s}_1} + 0.5\phi_{\text{s}_{n-1}} - 1.5\phi_{\text{s}_{n-1}}} \quad (22)$$

3.2.2. Hybrid Spectral — FV Scheme

Fast and accurate estimation of the solid phase lithium concentration, particularly its value at the surface of electrode particles is an inherent requirement of the layer optimisation procedure presented in Section 3. The high power densities that result from using low layer counts necessitate this requirement. It has been acknowledged that concentration calculations employing polynomial approximations such as those proposed in [47] lack fidelity at high charge/discharge rates [48]. Hence, a conventional full-order solution based on Fick's law of diffusion is appropriate.

With full-order solid phase diffusion dynamics, applying the FV scheme (that has been employed to discretise all through-thickness PDEs in the P2D model) results in a large system of equations. This is due to the requirement of using a high radial node density per spherical particle for improved accuracy. Consequently, the computational cost is high and simulation runtime becomes prohibitive when exploring the search space of all possible layer configurations. Moreover, with a cell-centered FV discretisation, it is non-trivial to directly apply the ionic flux boundary condition at the particle surface, since it involves extrapolation from at least two other nodes within the particle. While such extrapolations are acceptable in the axial dimension — particularly with high node densities providing small values of $\frac{\Delta x}{2}$ — they are undesirable in the radial dimension. This is because cell's open circuit and terminal voltages strongly depend on the concentration at the particle surface. Spectral methods offer a combination of high accuracy and speed while permitting the use of a lower number of radial discretisation nodes. To implement a spectral scheme on a non-periodic domain, a Chebyshev discretisation may be applied [49]. Bizeray *et al.* discretised all of the P2D model equations using this approach [50]. However, this entails a bi-directional mapping of all variables between the physical and Chebyshev domains, incurring computational overhead.

Here we propose the use of a hybrid formulation of the P2D model wherein a standard FV scheme in the axial dimension and a spectral scheme in the radial domain are used. By exploiting the natural separation of the axial and radial domains, we i) retain the ability to easily couple the molar flux density at the particle surface through reformulation of the boundary conditions of the solid diffusion PDE and ii) solve for solid-phase lithium concentration in the Chebyshev domain and locally transform to physical domain, without requiring system-wide Chebyshev reformulations. Although the proposed implementation does not globally employ a spectral scheme, the combined beneficial effects of radial-domain spectral scheme and automatic differentiation of system equations using CasADi [51] facilitates rapid simulation, enabling layer optimisation on short time-scales. Eqns (23)– (26) detail the steps leading to the reformulated solid phase diffusion and its associated boundary condition in the Chebyshev domain.

The Chebyshev collocation nodes defined on a 1D mesh in the radial direction are given by eqn (23) [49].

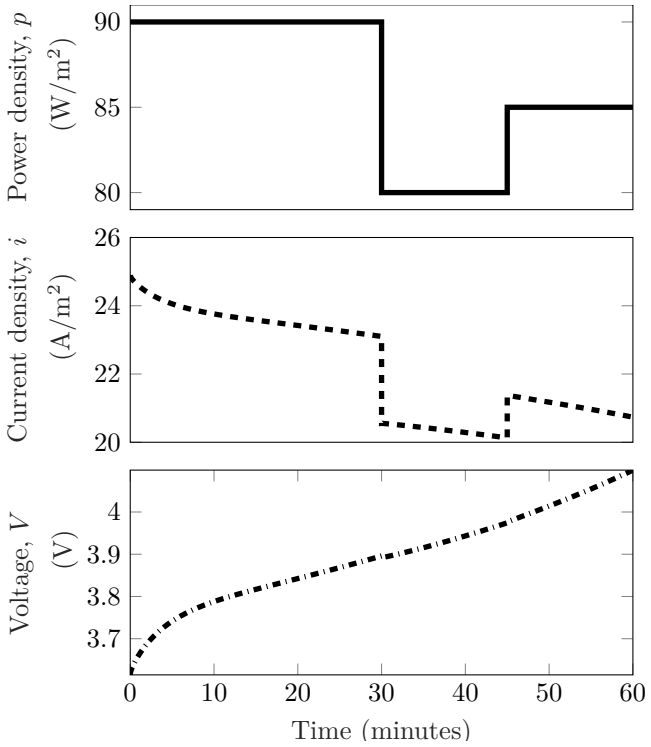

Figure 6 A positive (charging) power density is applied to a cell whose parameters are given in table 2 (top sub-plot), demonstrating the use of innate power density input. The current density (middle sub-plot) and cell voltage (bottom sub-plot) are solved by a DAE solver.

[4]In BOLD toolbox, the reformulated boundary condition is applied to the negative electrode.

$$\tilde{r} = \cos\left(\frac{i\pi}{N_r}\right), \qquad i = 0, 1, \ldots N_r \quad \tilde{r} \in [-1, 1] \tag{23}$$

Assuming constant diffusivity, and expanding the derivative in the standard form of the Fickian spherical diffusion equation for each particle (refer AppendixA) we obtain eqn (24), presented along with its Neumann boundary conditions. j is the molar flux density (mol m^{-2} s^{-1}) and R_p is the particle radius (m).

$$\frac{\partial c_s}{\partial t} = D_s^{\text{eff}}\left(\frac{\partial}{\partial r}\frac{\partial c_s}{\partial r} + \frac{\partial^2 c_s}{\partial r^2}\right) \qquad r \in [0, R_p] \tag{24}$$

$$\left.\frac{\partial c_s}{\partial r}\right|_{r=0} = 0 \tag{24a}$$

$$\left. D_s^{\text{eff}}\frac{\partial c_s}{\partial r}\right|_{r=R_p} = -j \tag{24b}$$

Mapping $r \in [0, R_p] \mapsto \tilde{r} \in [-1, 1]$,

$$r = \frac{R_p}{2}(\tilde{r} + 1) \tag{25}$$

Applying eqn (25) to eqn (24) whilst retaining c_s in the physical space yields eqn (26).

$$\frac{\partial c_s}{\partial t} = 4\frac{D_s^{\text{eff}}}{R_p^2}\left(\frac{2}{\tilde{r}+1}\frac{\partial c_s}{\partial \tilde{r}} + \frac{\partial^2 c_s}{\partial \tilde{r}^2}\right) \tag{26}$$

$$\left.\frac{\partial c_s}{\partial \tilde{r}}\right|_{\tilde{r}=-1} = 0 \tag{26a}$$

$$\left. 2\frac{D_s^{\text{eff}}}{R_p}\frac{\partial c_s}{\partial \tilde{r}}\right|_{\tilde{r}=1} = -j \tag{26b}$$

During the iterative solution process, the spatial gradients of solid phase lithium concentration in eqn (26) are not computed through an explicit differentiation procedure, but instead evaluated by pre-multiplying the concentration values at the collocation nodes by a Chebyshev differentiation matrix. This particular fact is responsible for the inherent reduction of simulation runtime achieved by introducing a spectral method. In the modified version of LIONSIMBA used in the layer optimisation methodology, differentiation matrices of suitable dimension as well as the Chebyshev collocation nodes are generated using the MATLAB function `cheb.m` [49].

4. Results and Discussion

4.1. xEV Configurations

The xEV parameters used in simulations are shown in tables 3a and 3b. Analysis of typical drive cycles (such as New European Driving Cycle (NEDC), Extra-Urban Driving Cycle (EUDC), Urban Dynamometer Driving Schedule (UDDS) and Highway Fuel Economy Driving Schedule (HWFET)) using these parameters reveals that their power demands on the battery pack are much lower than those required for acceleration and fast charging. The sign convention adopted for this work uses negative values for discharge. The largest magnitude peak and median discharge powers of various drive cycles were −50.83 kW (NEDC, EUDC) and −14.20 kW (HWFET), respectively. Accounting for the worst-case scenario wherein 100 % of braking energy is recovered, the largest magnitude peak and median charge powers were 43.13 kW (NEDC, EUDC) and 26.03 kW (EUDC), respectively. For a given layer configuration of the cells, which translates to a fixed vehicle mass, acceleration from standstill on a flat road demands −181.45 kW from the BEV battery pack. Comparatively, fast charging powers used in this work range from 50 kW to 135 kW. The lower value corresponds to the minimum of the definition of Level 3, off-board fast charging as discussed in [52]. The upper value corresponds to 35 % higher power than the maximum Level 3 rating given in [52]. This choice brings the fast charging goals in-line with the peak power capability of the present generation Tesla Superchargers [53, 54]. Simulations for both the BEV and PHEV confirmed that power demands of drive cycles are adequately small, so that they play no role in defining the peak power requirements for an xEV. Based on this analysis, while prima facie it appears that acceleration places the greatest burden on the pack, this may not be necessarily so. Several factors such as duration of peak power demand, voltage and SOC cut-off limits, need to be considered for a systematic pack design that adheres to specifications.

Table 3a Acceleration test parameters (common across xEV platforms)

Parameter	
Coefficient of drag for xEV body, C_d	0.31[a]
Frontal area of xEV, A_v (m^2)	2.40[b]
Acc. time dictated by standards, $t_{f,std}$ (s)	6.00[c]
Acc. time specified by manufacturer, $t_{f,man}$ (s)	6.50[d]
Speed, end of acc. (standards), $v_{f,std}$ (m s^{-1})	8.94[e]
Speed, end of acc. (manufacturer), $v_{f,man}$ (m s^{-1})	26.82[f]
Base speed of xEV, v_b (m s^{-1})	13.41[e]
Air density at acc. test conditions, ρ_{air} (kg m^{-3})	1.20[f]
Drivetrain efficiency, η_{dt}	0.75[g]
Payload, M_p (kg)	150.60[c]
Rolling resistance Coefficient of road surface, C_r	0.01[f]
Road gradient, Z	0.00[g]

[a] Ref [55]
[b] Calculated from typical BEV dimensions in [56].
[c] Ref [57] [d] Ref [58] [e] Ref [59] [f] Ref [60]
[g] Assumed

The maximum xEV pack voltage is 403.2 V, resulting from 96 series connected cells, using the cell V_{max} value from table 2. It is desirable to maintain voltage swing at the pack output within a controlled window of approximately 20 % in order to keep the downstream power electronics operating close to their peak efficiency. A minimum pack voltage of 336.0 V in the discharged state is therefore acceptable, with the corresponding V_{min} calculated and given in table 2. For acceleration tests, we set initial cell SOC to 40 %. This corresponds to the lower

Table 3b Acceleration test parameters (specific to each xEV)

Parameter	BEV	PHEV
Mass of xEV chassis, M_c (kg)	1340[a]	1438[b]
Mass of pack overhead (w/o cells), M_o (kg)	196.4[a]	65.5[c]
Upper cutoff SOC of cell, z_{max} (%)	95[d]	90[d]
Lower cutoff SOC of cell, z_{min} (%)	5[d]	30[e]

[a] Calculated, based on.[61] [b] Calculated, based on.[61, 62]
[c] Calculated, see section 4.1 [d] Assumed [e] Ref.[60]

extreme of the test criterion, (50 ± 10) %, as per the SAE J1666 standard [57]. This minimises the overhead available to accommodate the polarisation in terminal voltage before the lower cell voltage limit is hit, thus ensuring a conservative design. For the BEV, we initiate fast-charging in Constant Power (CP) mode starting at 20 % SOC. As with the BEV, PHEV acceleration testing was conducted with initial SOC of 40 %. However, we subjected the PHEV to fast-charging in CP mode from an initial SOC of 30 %, i.e. 10 % higher than the BEV. This is to account for PHEV pack's need to undergo a much larger number of charge-discharge cycles, prompting vehicle manufacturers to use a smaller SOC window. We fast charged both xEV platforms to the same 80 % SOC target in CP mode. Since this target is lower than the upper SOC cut-off, z_{max}, for both the BEV and the PHEV, fast charging could be allowed to continue beyond the CP phase using the charging algorithm's square-wave pulsing, but is prevented from doing so in the interest of faster run-times as described in 3.1.

For both xEV platforms, the vehicle mass includes two passengers (75.3 kg per passenger) and omits pack mass, but is otherwise all-encompassing [57]. Vehicle mass for the PHEV differs from that for the BEV only due to the addition of a range-extending ICE whose mass value is based on the GM Ecotec series from the company's Volt PHEV [62]. Pack mass consists of i) pack overhead, accounting for the pack structure and all non-cell components such as thermal management hardware, and ii) the mass of all the cells within. We estimated BEV pack overhead by subtracting the computed mass of typical cells from the mass of a complete Bolt BEV pack given in [61]. PHEV pack overhead is equivalent to BEV pack overhead scaled proportionally by the magnitude of the reduction in cells between the two platforms. As described in 3.1, the mass of the cells within the pack is a function of the number of layers in each cell, and was dynamically recalculated throughout simulations.

4.2. BEV Acceleration Pathway

The results that follow were obtained using the methodology illustrated in Fig. 3 and described throughout 3. All simulations were conducted with cells initially in their equilibrium state. We simulated BEV acceleration at a worst-case rate of $4.13\,\mathrm{m\,s^{-2}}$, corresponding to the manufacturer-derived v_f and t_f in table 3a. We completed acceleration simulations for the combinations of (T_{init}, T_{sink}) given in table 4. Simulation at these combinations constitutes a set of extremes that is sufficient to describe the xEV thermal design space given by the standards and discussed in 3. Whilst also an extreme, the combination $T_{init} = 15\,°C$, $T_{sink} = 49\,°C$ has been omitted since it is, in reality, implausible that the pack temperature be so much below that of the coolant. We included the typical 25 °C scenario for completeness, although since it lies within the bounds of the other combinations, it does not play a role in defining the optimal layer configuration. Through application of the search algorithm, the search space given by $n_{min} \leq n \leq n_{max}$ was explored and n^{acc}_{opt} determined for the BEV. The results are given in table 4. Power density p^{acc} is substantial in cells with low numbers of layers, beginning at $-14.92\,\mathrm{kW\,m^{-2}}$ for a single-layer cell configuration in a pack required to deliver −180.0 kW during BEV acceleration. Increasing n from n_{min} drives up A_{cell}, in turn inducing an exponential decrease in p^{acc}. As n increases the total mass actually increases slightly, as less dense active materials are replaced with more dense inactive materials such as copper current collectors, however, this effect on the overall results is trivial. As hypothesized, we observe that the enormous power densities associated with low numbers of layers induce large negative overpotentials, immediately causing cell terminal voltage to drop below V_{min} and that layer configuration to exhibit a SOF of zero. i.e. those layer configurations are incapable of satisfying the acceleration requirements.

Table 4 xEV acceleration test results

(T_{init}, T_{sink}) °C	(38, 5)	(38, 49)	(25, 25)	(15, 5)
n^{acc}_{opt}, BEV	20	21	23	25
n^{acc}_{opt}, PHEV	55	57	63	69

The number of layers required to achieve a unity SOF is least for the highest initial cell temperature, then gradually increases as T_{init} decreases. Moreover, so long as cell temperature does not pose the risk of exceeding T_{max}, higher initial cell temperatures are beneficial because they minimise the negative overpotential experienced during discharge, permitting a lower value of n to meet the $V(t_f) \geq V_{min}$ criterion. The reduction in overpotential occurring with higher values of T_{init} outweighs the small loss of Open Circuit Potential (OCP) at higher values of T_{init}, which alone acts to reduce the overhead available to accommodate polarisation. It follows that a more energy-dense layer configuration can be afforded if the xEV manufacturer can accurately determine the minimum sink temperature during operation, and the associated additional vehicle range enjoyed. Across all temperature combinations, the largest departure from T_{init} experienced by a BEV cell is a 0.48 °C increase. Logically, this occurs when the rate of heat transfer from the thermal management system is greatest, i.e. for the temperature combination with the greatest positive value of $(T_{sink} - T_{init})$, which is $T_{init} = 38$, $T_{sink} = 49$ °C. Consequently, we observe that a single acceleration event does little to heat the BEV battery pack, and cells remain close to their initial temperature throughout the test. In similarity to the small magnitude of the cell temperature perturbation, cell SOC is depleted only by a maximum value

of 0.32 %, so that the lower cut-off voltage is by a large margin the limiting property when defining the layer configuration via acceleration. Upon the BEV reaching $v_{\mathrm{f,man}}$ and beginning the cruise phase of the acceleration test, $P_{\mathrm{batt}}^{\mathrm{acc}}$ falls in absolute terms from −627.6 W to −58.5 W in the case of the 25 layer cell at $T_{\mathrm{init}} = 15\,^{\circ}\mathrm{C}$, $T_{\mathrm{sink}} = 5\,^{\circ}\mathrm{C}$. We observe a corresponding, near-instantaneous and partial recovery of terminal voltage from a value of 3.51 V, barely above V_{min}, to a plateau of approximately 3.74 V. The result corroborates the theory that the lower power requirement and short duration of the cruise phase does not, for all reasonable values of a_{man}, influence the optimal layer configuration obtained via acceleration tests. This trend holds across all temperature combinations tested. $n_{\mathrm{opt}}^{\mathrm{acc}}$ for the BEV is thus greatest at $T_{\mathrm{init}} = 15\,^{\circ}\mathrm{C}$, $T_{\mathrm{sink}} = 5\,^{\circ}\mathrm{C}$ where the largest overpotential occurs as a result of a reduced rate of electrochemical reaction at this relatively low temperature. Since it is necessary to choose the greatest n — that layer configuration corresponding to the worst case thermal environment the BEV will witness — we deem $n = 25$ to be the cardinal optimal layer configuration arising from acceleration tests for the BEV platform. Therefore, $n = 25$ is the maximum-energy-density cell configuration permissible, representing the design choice where BEV range is maximised subject to the constraint of meeting the desired acceleration requirements.

4.3. BEV Fast Charging Pathway

For the fast charging process, we explored the search space given by $n_{\mathrm{min}} \leq n \leq n_{\mathrm{max}}$ and determined $n_{\mathrm{opt}}^{\mathrm{fastchg}}$ for the BEV for each charging power presented in Fig. 7. Each quadrant within the figure represents a map of the thermal design space bounded by the set of extreme temperature combinations given earlier in this section. The optimal layer configuration arising from fast charging, $n_{\mathrm{opt}}^{\mathrm{fastchg}}$, for the BEV is again determined solely by these bounding temperature scenarios, represented in the four corners of each quadrant in Fig. 7. Simulating the extremes alone expedites the optimisation process and rapidly provides the cardinal solution, and we provide here the maps for the purposes of inference and discussion. The maps represent over 264 different sets of conditions, and for each set of conditions an average of ~50 simulated fast charges occurred, therefore representing over 10,000 model runs, demonstrating the need for an efficient model to undertake an optimisation process of this type. The values contained within the maps are the values of $n_{\mathrm{opt}}^{\mathrm{fastchg}}$ corresponding to that combination of $(T_{\mathrm{init}}, T_{\mathrm{sink}})$. That is, they represent the minimum number of cell layers required to fast charge the pack under CP conditions to the target SOC, z^*, while simultaneously i) preventing lithium plating of the negative electrode particles, ii) limiting cell temperature to no more than T_{max} and iii) maintaining cell voltage less than or equal to V_{max}. Cell design with these configurations results in an optimal balance of energy and power, such that the maximum-energy density and BEV range is obtained, subject to meeting the fast charging targets.

Box colour within quadrants represents the quantity of charge added, q, given in Ah, to a single cell in the pack for that layer configuration. We show that if the layers are optimally configured for the lowest charging rate, the BEV cells accept 33.9 Ah to 38.0 Ah (mean: 36.5 Ah) — equivalent, at the potential corresponding to the completion of charge, to adding 38.7 kWh to 43.4 kWh of energy to the pack. In comparison, for optimally configured cells at each increased charging power we demonstrate that the cells receive less charge; 32.2 Ah to 37.4 Ah (mean: 34.6 Ah), 30.6 Ah to 35.3 Ah (mean: 33.1 Ah) and 30.0 Ah to 34.0 Ah (mean: 32.0 Ah) added at 80 kW, 110 kW and 135 kW, respectively. Furthermore, $n_{\mathrm{opt}}^{\mathrm{fastchg}}$ trends upwards with higher charging powers. This effect is pronounced in the non-linear and decreasing rate increase of the mean values of $n_{\mathrm{opt}}^{\mathrm{fastchg}}$; 50, 61, 70 and 76 layers required on average for each of the 50 kW, 80 kW, 110 kW and 135 kW fast charging powers, respectively. As the charging power increases so does the overpotential for a given n, and thus the minimum value of n required to maintain $V_{\mathrm{t}} \leq V_{\mathrm{max}}$ increases as charging power increases. That is, increasingly more interfacial surface area is required to absorb the higher applied powers. Once n exceeds this minimum, the impact of the V_{max} constraint lessens and that constraint is superseded in its impact by the dual requirement of satisfying the criteria $c_s^* < c_{\mathrm{s,sat}}$ and $z(t) > z^*$. It is challenging to satisfy the two criteria simultaneously owing to the rate-limiting diffusion of lithium in the solid phase of the negative electrode, which induces the undesirable saturation of the particle surface at values of $z(t) < z^*$ for low n, correspondingly producing a SOF of zero. Higher charging powers instigate steeper concentration profiles in the negative electrode particles and lead to more rapid surface saturation, exacerbating the difficulty of reaching z^* without plating, and hence forcing the search algorithm to increment n until $n_{\mathrm{opt}}^{\mathrm{fastchg}}$ is determined, wherein both $z(t) > z^*$ and $c_s^* < c_{\mathrm{s,sat}}$ criteria can be simultaneously satisfied. Interestingly, this accentuates an obscure, but crucial, link between solid phase diffusion rates and xEV range. While diffusion rate limitations are most frequently considered in the context of xEV power alone, we assert that they play an influential role in defining the maximum range of an xEV. Since it is the solid phase diffusion rate that, for a given fast charging power and layer count, n, defines the concentration gradient, and therefore the onset of lithium plating. According to the layer configuration methodology — wherein n must be sufficiently great to prevent plating — increased diffusion rates permit cells featuring lower numbers of layers (providing correspondingly increased nominal pack capacity and vehicle range) accept a given fast charging power without succumbing to plating. A similar situation exists when the direction of power flow is reversed during acceleration, where $n_{\mathrm{opt}}^{\mathrm{acc}}$ is defined by the onset of terminal voltage collapse — a phenomenon that is attenuated with faster solid phase diffusion, permitting higher energy density layer configurations. Consequently, we emphasize the importance of high solid phase diffusion rates not only for minimising fast charge and acceleration times, but for maximising xEV range.

The upper-right quadrant in Fig. 8, corresponding to BEV fast charging under CP conditions, aids in further inference of the relationship between charge passed, q, charging power and n for any single $(T_{\mathrm{init}}, T_{\mathrm{sink}})$ combination. Nominal cell capacity, Q_{n}, is shown to be linearly driven down in monotonic fashion

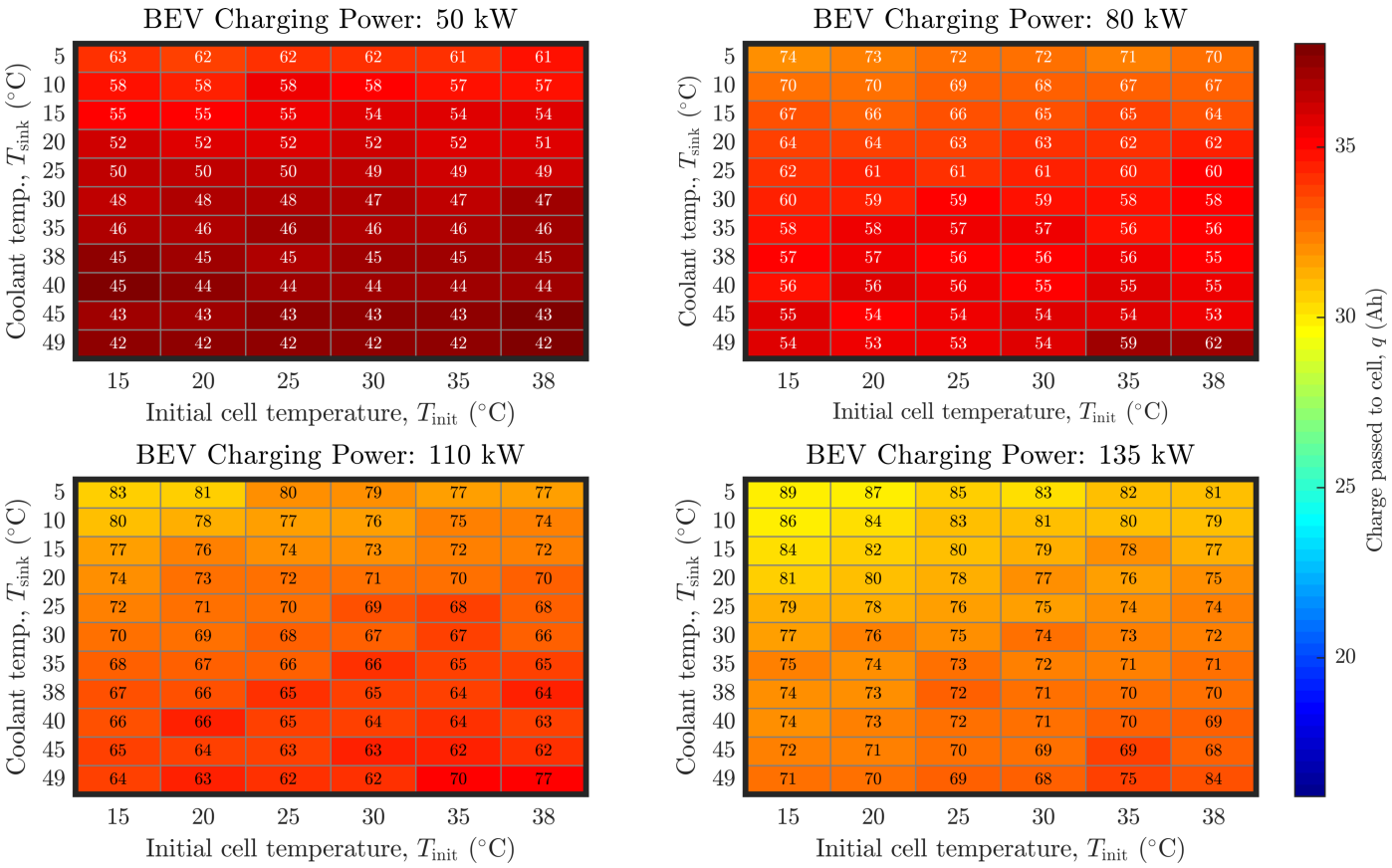

Figure 7 Optimal cell layer configurations for the BEV, presented for a range of fast charging powers and thermal conditions.

with the addition of layers, as expected. At the lowest values of n, no charge is passed to the cell because excessive power densities create large overpotentials that instantaneously drive the terminal voltage above V_{max}. Above a critical value of n, the cell can absorb the power without immediately exceeding V_{max}. For all charging powers, continuing to increase n yields an increase in charge passed because the power density reduces at a greater rate than nominal capacity, as illustrated in Fig. 4. As it does so, the impact of the V_{max} criterion lessens and that criterion is superseded by the $c_s^* < c_{\text{s,sat}}$ criterion, such that plating prevention becomes the limiting factor on the quantity of charge being transferred. Maximum charge passed occurs at higher values of n for higher charging powers because greater power densities require a greater number of layers to absorb the same charge as a lower number of layers when operating immediately below the lithium plating threshold. This charge-rate dependency is represented by the rightward-shifting curves as charging rates grow. Charge passed reaches a maximum at the lowest number of layers whereby the maximum permissible cell SOC has been attained, and is reflected in the inflection points of the curves. For values of n above the power-dependent inflection, q exhibits a linear decrease with increasing n for all levels of charging power, albeit at a lower rate than Q_{n}. This is a direct result of the nature of the fixed SOC target z^*, which, for a given rate of CP charging, ensures that the absolute quantity of charge passed reduces as Q_{n} reduces. That is, the reducing nominal capacity tends to drag downwards the usable capacity, as well. Since Q_{n} reduces as layers are added to accommodate higher charging powers, charge passed is thus necessarily less when faster charging rates are employed and is a cost of obtaining a reduced charging time. Notably, the differing rates of loss, such that $\lim_{n \to n_{\text{max}}}(Q_{\text{n}}(n) - q(n)) = 0$, results in the total charge passed representing a larger fraction of nominal capacity for more rate-capable cells, and yields concomitantly greater utilisation of the active material. The implication is clear; if the pack is designed with optimally-configured cells for relatively high-power fast charging, more efficient use is made of the pack's capacity when charging between $z_{\text{min}}^{\text{fastchg}}$ and z^*, than if the pack's cells are optimally-configured for relatively low-power fast charging.

For both methodology pathways, the thermal environment has a substantial influence on the optimal cell layer configuration with $n_{\text{opt}}^{\text{fastchg}}$ varying as function of both T_{init} and T_{sink}, emphasizing the importance of conducting thermally-coupled simulations. Similar to the results of acceleration, we determined that, for all charging powers simulated, $n_{\text{opt}}^{\text{fastchg}}$ is a maximum for the lowest temperature combination, $T_{\text{init}} = 15\,°\text{C}$, $T_{\text{sink}} = 5\,°\text{C}$ — again a consequence of the sluggish rate of electrochemical reaction at these lower temperatures. It is however premature to consider the lowest temperature scenario to be unconditionally pre-eminent.

At 50 kW, for any given value of T_{init} we observe a decreasing-rate, positive correlation between $n_{\text{opt}}^{\text{fastchg}}$ and T_{sink} such that their

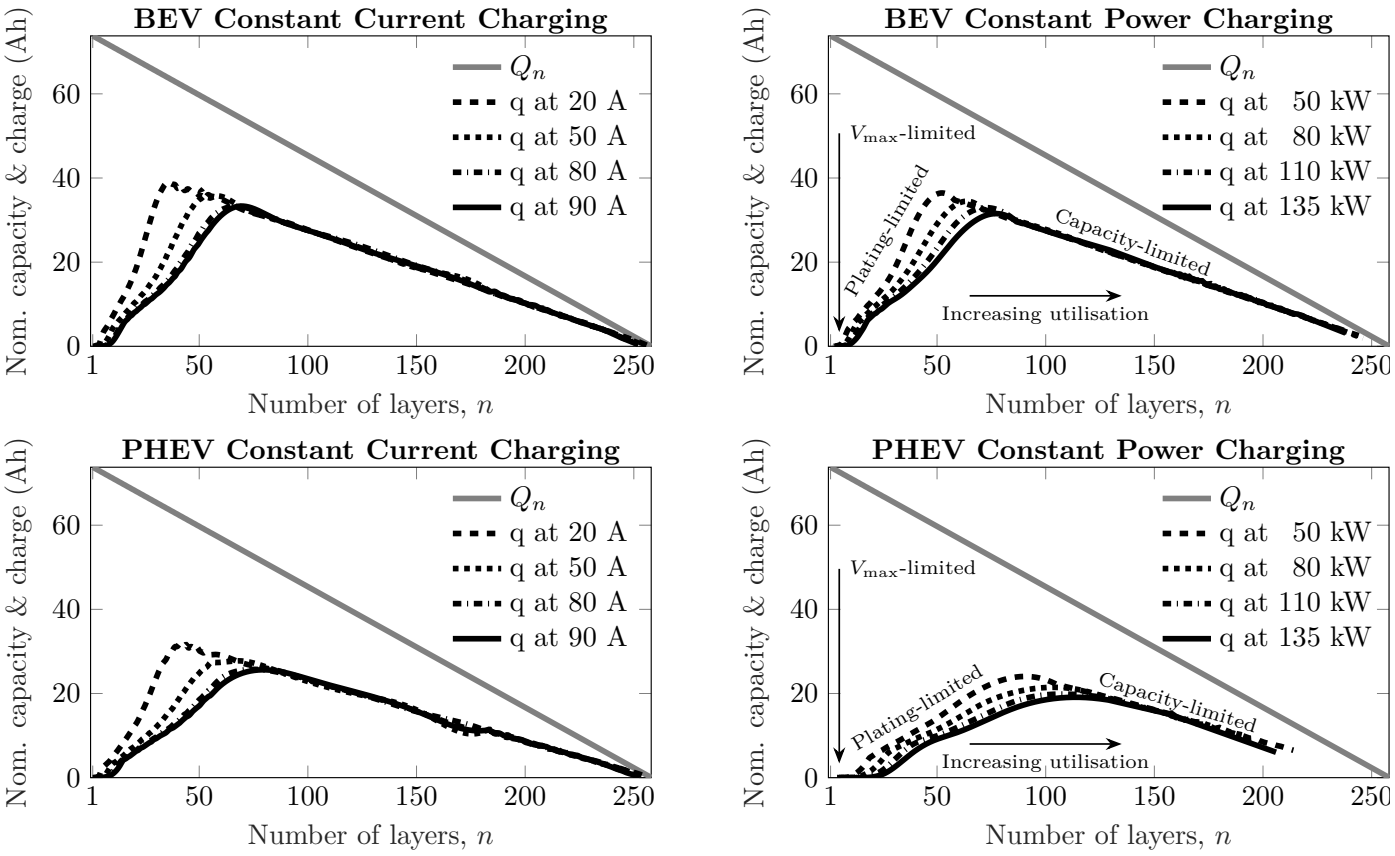

Figure 8 The plots in the right column show the nominal cell capacity and charge passed during xEV CP charging. Increased rate capability and cell utilisation are positively correlated with n, while the maximum-q layer configuration clearly shifts to higher values of n with increasing charging powers. The plots in the left column depict galvanostatic charging scenarios at various currents to highlight the similarity with the CP process. All data obtained at $T_{\text{init}} = 25\,^{\circ}\text{C}$, $T_{\text{sink}} = 25\,^{\circ}\text{C}$.

relationship is described by a parabola. Higher coolant temperatures permit the use of more energy dense layers configurations and are therefore favourable for BEV AER. However, as charging power increases, so does the rate of self-heating and the difficulty of heat rejection such that at 80 kW and above, $n_{\text{opt}}^{\text{fastchg}}$ no longer constantly decreases with increasing sink temperatures. Instead, at high sink temperatures, $n_{\text{opt}}^{\text{fastchg}}$ increases again as the $T(t_{\text{f}}) < T_{\text{max}}$ criterion becomes influential, requiring power density reductions to limit the value of $T(t_{\text{f}})$. Notably however, while increasing $n_{\text{opt}}^{\text{fastchg}}$ has the net effect of attenuating $T(t_{\text{f}})$, the temperature-limiting effect is to a small extent hindered by the negative, linear correlation between n and the specific heat capacity of the cell. This occurs because the rate of decline of c_{j} with the loss of active material dominates the increase in c_{j} occurring with the addition of inactive material. Hence, the faster the charging rate, the smaller the difference between the optimal layer configuration required for operation at the lowest and highest temperature extremes. This is most evident when differencing the optimal layer configurations for the $T_{\text{init}} = 15\,^{\circ}\text{C}$, $T_{\text{sink}} = 5\,^{\circ}\text{C}$ and $T_{\text{init}} = 38\,^{\circ}\text{C}$, $T_{\text{sink}} = 49\,^{\circ}\text{C}$ scenarios, for each of the 50 kW and 135 kW charging powers. As charging power increases, so does the challenge of intercalating lithium without plating. Hence, the rate of decline of $n_{\text{opt}}^{\text{fastchg}}$ with increasing T_{init} steepens as charging power is increased because higher initial pack temperatures lessen the propensity to plate lithium by accelerating the rate of reaction. In spite of the substantially lower magnitude of the pack powers during fast charging relative to those required for xEV acceleration, it is the fast charging that defines the higher (at 89 versus 25 layers for acceleration), and therefore cardinal, optimal layer configuration for the BEV.

4.4. Common Module Design

Thus far, we have demonstrated a cell design methodology to maximise xEV AER for a given set of acceleration and fast charging targets, providing a viable, model-led alternative to reiterative empirical testing. By maintaining a fixed set of exterior cell dimensions and varying only the layer configuration between the BEV and PHEV presented above — we establish the usefulness of the optimisation methodology for common battery pack module design. Simulating acceleration of the PHEV with the specifications described at the beginning of Fig. 4 yields the maximum energy density layer configurations, $n_{\text{opt}}^{\text{acc}}$, in the lower row of table 4. The smaller PHEV pack mandates that acceleration power requirements are distributed across fewer cells,

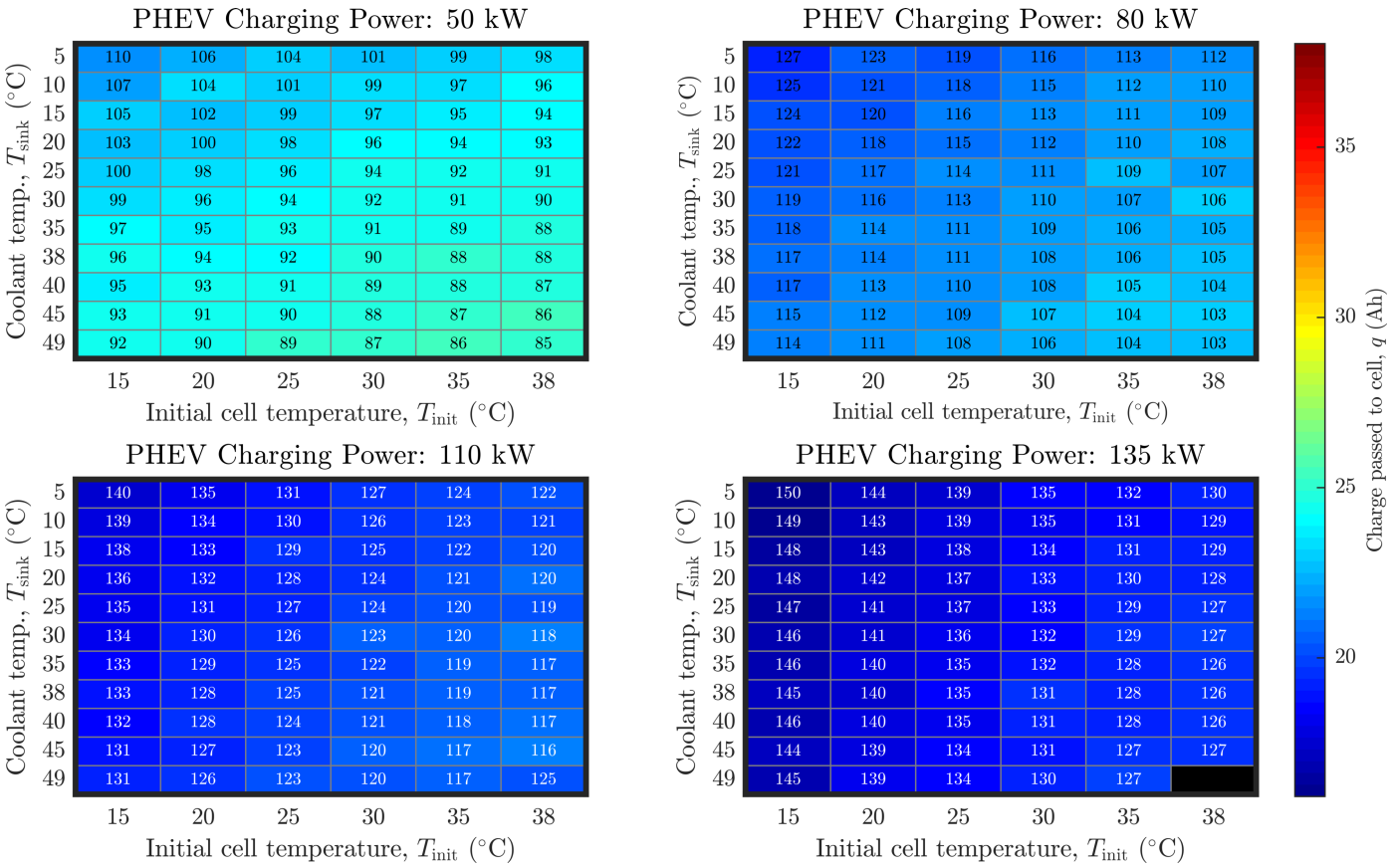

Figure 9 Optimal cell layer configurations for the PHEV, presented for a range of fast charging powers and thermal conditions.

and the per-cell power densities are correspondingly larger[5] than those for the BEV. Accordingly, the number of layers required for the PHEV cell to satisfy the acceleration requirements are, on average, 2.7 times greater than for a BEV cell. We observe that the number of layers required for PHEV fast charging are also greater than those required for acceleration, and thus fast charging represents the toughest test of PHEV cell rate capability. Fig. 9 depicts the optimal layer configurations for the PHEV derived through fast charging. By considering only charge passed rather than total charge available in the pack, the maps of Fig. 7 and Fig. 9 are de-biased with respect to the unequal initial SOC of the two xEV platforms, facilitating comparison of q data between the two figures. The trend of the coldest thermal scenario mandating the highest active surface area, and therefore the cardinal layer configuration, is upheld in the case of the PHEV. However, there are important differences between the results for each xEV platform. Substantially less charge is passed to the PHEV pack than to the BEV pack, owing to the lower absolute quantity of charge necessary to reach the 80 % target of the smaller pack. This reduction in charge passed is magnified because the reduction in pack capacity between BEV and PHEV doesn't arise solely from the removal of two parallel strings of modules, but also from the loss of active material in cells which must contain greater numbers of layers to accommodate a charging power that is distributed across one-third the number of cells. Charging the PHEV and the BEV at the same rates results in lower charging times for the relatively small capacity hybrid, and simultaneously amplifies the difficulty of thermal management at high ambient temperatures that became apparent with the BEV. The black cell in the lower-right corner of the lower-right quadrant in Fig. 9 arises because no layer configuration exists whereby the power density can be made sufficiently small that, at $T_{\text{init}} = 38\,°\text{C}$, $T_{\text{sink}} = 49\,°\text{C}$ this thermal management system can satisfy the criterion $T(t_{\text{f}}) < T_{\max}$.

Crucially, the design maps within Fig. 9 demonstrate that the different demands of an alternative xEV platform can be satisfied using a cell of identical external dimensions, and hence, using a common xEV battery pack module design. Furthermore, the layer configuration is determined rapidly, at low cost, and is optimal in terms of its energy density, providing maximised PHEV AER.

5. Conclusions

We have demonstrated a methodology to optimise the energy density of cells for xEV platforms utilising fast-charging at the lithium plating threshold. In doing so, we have presented a design toolbox, BOLD, that offers xEV and cell manufacturers the opportunity to eliminate cell over-engineering, increasing xEV

[5] Larger, but not proportionally by the reduction in the cell count because the different mass of the PHEV relative to the BEV results in unequal powers being required at the pack level. Only during fast charging is the power density in PHEV cells exactly scaled by the reduction in the number of cells.

AER, and to replace the time-consuming experimental, reiterative determination of layer configurations, thereby reducing EV cost. Furthermore, we have demonstrated how common module design for multiple xEV platforms can be achieved by varying only the layer configurations within cells, producing optimised battery packs containing identical modules for each vehicle platform. The technique has the potential to reduce both the cost and time expenditure required by an automotive OEM to add a new xEV to their product range, thereby de-risking and expediting the transition to cleaner, de-carbonised transport. We enhanced the standard form of the P2D model, developing a direct power density input boundary condition on the solid-phase potential PDE, thereby facilitating more accurate and facile modelling of vehicle drive cycles, acceleration and power-based charging. Using this model, we showed that for modern xEV platforms requiring Level 3 fast charging, it is the fast charging process that defines the optimal layer configuration, superseding drive cycle requirements in importance. As fast charging powers are expected to climb at a much greater rate than acceleration times are expected to fall for future electric vehicles, we expect that it will continue to play the dominant role in defining optimal layer configurations than xEV acceleration. Beyond demonstrating that, for a majority of thermal scenarios, the rate of lithium intercalation into the negative electrode is the limiting factor on the rate of charge addition to the battery pack, we demonstrated how it ultimately determines the AER of the EV. Consequently, we stress the importance — for both xEV range and for future research agendas — of focusing materials development efforts on the advancement of negative electrode materials exhibiting higher solid phase diffusion coefficients, particularly at low temperatures. Pursuing improvements to AER in a such a way — by enabling low layer-count configurations and improved energy density at the cell level — may prove faster and more fruitful than directly pursuing improvements to the gravimetric energy density of electrode materials. The returns available through such a re-balancing of resources merits further investigation. We additionally illustrated how, at relatively high operating temperatures, the plating threshold limitation on charging rate is deposed, with the charging rate instead becoming limited by the relative rates of heat accumulation and rejection. As increasingly short duration fast charging is sought, the thermal management system's ability to extract heat from the cells will play an increasingly large role in determining xEV AER by permitting lower-layer-count configurations to accept high power densities. Finally, in providing this model-driven approach, we have solved one component of a problem that plagues the battery industry — that is, the expensive use of reiterative empirical testing to determine layer configurations. To obtain the fullest benefits, we advocate close collaboration between EV and cell manufactures, facilitating the tailoring of cell designs to an xEV's fast charging and acceleration targets. We believe such an approach to be a pre-requisite to avoid cell over-engineering.

Future work could include refinements to the tools employed in the layer optimisation methodology. The solid phase diffusion coefficient could be made a function of SOC to provide an increase in the accuracy of the plating threshold predictions. The thermal model could be improved by adaptively varying the lumped thermal conductivity as a function of the number of cell layers, since additional current collectors provide an increase in the number of thermally-conductive pathways along the cell length. Future work could also include extensions of the layer optimisation methodology, such as the impact of increased power densities on the rate of cell degradation, assigning a cost function to energy density maximisation and enabling the design engineer trade xEV AER at the start of life with its rate of decline throughout the life of the vehicle. The usefulness of the optimisation methodology is also limited by the ease and cost of parametrising the underlying physics based model, and hence this should also be a priority for future research.

Acknowledgements

Funding: This work was supported by the UK Engineering and Physical Sciences Research Council (EPSRC), Jaguar Land Rover Ltd. [industrial CASE award]; and Imperial College London [President's PhD Scholarship].

These funding sources had no involvement in this study, manuscript preparation or decision to submit for publication.

Declaration of Interest

There are no conflicts or interests to declare.

Nomenclature

η	Overpotential (V)
κ_{eff}	Effective electrolyte conductivity (S m^{-1})
CC	Current collector
ϕ_{e}	Electrolyte phase potential (V)
ϕ_{s}	Solid phase potential (V)
σ_{eff_j}	Effective electronic conductivity (S m^{-1})
$\tilde{r}$	Displacement along P2D, radial axis, Chebyshev domain (m)
A_{cell}	Total electrochemically active surface area within the cell (m^2)
A_{tabs}	Combined surface area of cell tabs (m^2)
c	Specific (gravimetric) heat capacity $\text{J kg}^{-1}\ \text{K}^{-1}$
D^{eff}	Effective electrolyte diffusivity ($\text{m}^2\ \text{s}^{-1}$)
$D_{\text{s}}^{\text{eff}}$	Effective electrode diffusivity ($\text{m}^2\ \text{s}^{-1}$)
j	Ionic flux ($\text{mol m}^{-2}\text{s}$)
$k_{\text{r}}^{\text{eff}}$	Effective reaction rate constant
n_{feas}	A number of layers with a unity SOF
Q_{pol}	Heat generation due to polarisation (W)
r	Displacement along P2D, radial axis, physical domain (m)

T	Lumped cell temperature (K)
U	Cell open circuit potential (V)
V	Cell terminal voltage (V)
x	Displacement along through–thickness axis (m)
$x_{\mathrm{neg/Cucc}}$	Negative electrode–current collector interface
$x_{\mathrm{pos/Alcc}}$	Positive electrode–current collector interface

AppendixA. P2D Model Equations

Electrochemical model equations:

$$\varepsilon_l \frac{\partial c_\mathrm{e}(x,t)}{\partial t} = \frac{\partial}{\partial x}\left(D_l^\mathrm{eff}\frac{\partial c_\mathrm{e}(x,t)}{\partial x}\right) + a_l(1-t_+^0)j(x,t) \qquad l \in \{\mathrm{pos,sep,neg}\} \tag{A.1}$$

$$\left.\frac{\partial c_\mathrm{e}(x,t)}{\partial x}\right|_{\substack{x=x_{\mathrm{pos/Alcc}}\\ x=x_{\mathrm{neg/Cucc}}}} = 0 \tag{A.1a}$$

$$\frac{\partial c_\mathrm{s}(r,t)}{\partial t} = \frac{1}{r^2}\frac{\partial}{\partial r}\left(r^2 D_{\mathrm{s}_l}^\mathrm{eff}\frac{\partial c_\mathrm{s}(r,t)}{\partial r}\right) \qquad l \in \{\mathrm{pos,neg}\} \tag{A.2}$$

$$\left.\frac{\partial c_\mathrm{s}(r,t)}{\partial r}\right|_{r=0} = 0 \tag{A.2a}$$

$$\left.\frac{\partial c_\mathrm{s}(r,t)}{\partial r}\right|_{r=R_\mathrm{p}} = -\frac{j(x,t)}{D_\mathrm{s}^\mathrm{eff}} \tag{A.2b}$$

$$a_\mathrm{s}F j(x,t) = -\frac{\partial}{\partial x}\left(\kappa_{\mathrm{eff}_l}\frac{\partial \phi_\mathrm{e}(x,t)}{\partial x}\right) + \frac{\partial}{\partial x}\left(\kappa_{\mathrm{eff}_l}T(t)\frac{2R\left(1-t_+^0\right)}{F}\frac{\partial \ln c_\mathrm{e}(x,t)}{\partial x}\right) \qquad l \in \{\mathrm{pos,sep,neg}\} \tag{A.3}$$

$$\left.\frac{\partial \phi_\mathrm{e}(x,t)}{\partial x}\right|_{x=x_{\mathrm{pos/Alcc}}} = 0 \tag{A.3a}$$

$$\partial\phi_\mathrm{e}(x,t)|_{x=x_{\mathrm{neg/Cucc}}} = 0 \tag{A.3b}$$

$$j(x,t) = 2k_{\mathrm{r}_l}^\mathrm{eff}\sqrt{c_\mathrm{e}(x,t)c_{\mathrm{s}_l}^*\left(c_{\mathrm{s,max}_l}-c_{\mathrm{s}_l}^*\right)}\sinh\left(\frac{0.5F}{RT(t)}\eta_l(x,t)\right) \qquad l \in \{\mathrm{pos,neg}\} \tag{A.4}$$

$$\eta_l(x,t) = \phi_\mathrm{s}(x,t) - \phi_\mathrm{e}(x,t) - U_l(\theta_l) \qquad l \in \{\mathrm{pos,neg}\} \tag{A.5}$$

$$\frac{\partial}{\partial x}\left(\sigma_{\mathrm{eff}_l}\frac{\partial \phi_\mathrm{s}(x,t)}{\partial x}\right) = a_\mathrm{s}F j(x,t) \qquad l \in \{\mathrm{pos,neg}\} \tag{A.6}$$

$$\sigma_{\mathrm{eff_{neg}}}\left(\phi_\mathrm{s}(x,t)\frac{\partial \phi_\mathrm{s}(x,t)}{\partial x}\right)_{x=x_{\mathrm{neg/Cucc}}} - \sigma_{\mathrm{eff_{pos}}}\left(\phi_\mathrm{s}(x,t)\frac{\partial \phi_\mathrm{s}(x,t)}{\partial x}\right)_{x=x_{\mathrm{pos/Alcc}}} = p \tag{A.6a}$$

$$\sigma_{\mathrm{eff_{pos}}}\left.\frac{\partial \phi_\mathrm{s}(x,t)}{\partial x}\right|_{x=x_{\mathrm{pos/Alcc}}} = -i \tag{A.6b}$$

$$\sigma_{\mathrm{eff}_l}\left.\frac{\partial \phi_\mathrm{s}(x,t)}{\partial x}\right|_{\substack{x=x_{\mathrm{pos/sep}}\\ x=x_{\mathrm{neg/sep}}}} = 0 \tag{A.6c}$$

$$U_\mathrm{pos} = \frac{-4.656 + 88.669\theta_\mathrm{pos}^2 - 401.119\theta_\mathrm{pos}^4 + 342.909\theta_\mathrm{pos}^6 - 462.471\theta_\mathrm{pos}^8 + 433.434\theta_\mathrm{pos}^{10}}{-1 + 18.933\theta_\mathrm{pos}^2 - 79.532\theta_\mathrm{pos}^4 + 37.311\theta_\mathrm{pos}^6 - 73.083\theta_\mathrm{pos}^8 + 95.96\theta_\mathrm{pos}^{10}} + \left(T(t)-T_\mathrm{sink}\right)\frac{\partial U_\mathrm{pos}}{\partial T} \tag{A.7}$$

$$U_\mathrm{neg} = 0.7222 + 0.1387\theta_\mathrm{neg} + 0.029\theta_\mathrm{neg}^{0.5} - \frac{0.0172}{\theta_\mathrm{neg}} + \frac{0.0019}{\theta_\mathrm{neg}^{1.5}} + 0.2808e^{(0.9-15\theta_\mathrm{neg})} - 0.7984e^{(0.4465\theta_\mathrm{neg}-0.4108)} + (T(t)-T_\mathrm{sink})\frac{\partial U_\mathrm{neg}}{\partial T} \tag{A.8}$$

$$\frac{\partial U_\mathrm{pos}}{\partial T} = -0.001\frac{0.199521039 - 0.928373822\theta_\mathrm{pos} + 1.3645506890000003\theta_\mathrm{pos}^2 - 0.61154489399999998\theta_\mathrm{pos}^3}{1 - 5.661479886999997\theta_\mathrm{pos} + 11.47636191\theta_\mathrm{pos}^2 - 9.824312135999998\theta_\mathrm{pos}^3 + 3.048755063\theta_\mathrm{pos}^4} \tag{A.9}$$

$$\frac{\partial U_{\text{neg}}}{\partial T} = 0.001\frac{w}{y} \tag{A.10}$$

$$\begin{aligned} w = {} & 0.005269056 + 3.299265709\theta_{\text{neg}} - 91.79325798\theta_{\text{neg}}^2 + 1004.911008\theta_{\text{neg}}^3 \\ & - 5812.278127\theta_{\text{neg}}^4 + 19329.7549\theta_{\text{neg}}^5 - 37147.8947\theta_{\text{neg}}^6 + 38379.18127\theta_{\text{neg}}^7 - 16515.05308\theta_{\text{neg}}^8 \end{aligned} \tag{A.10a}$$

$$\begin{aligned} y = {} & 1 - 48.09287227\theta_{\text{neg}} + 1017.234804\theta_{\text{neg}}^2 - 10481.80419\theta_{\text{neg}}^3 + 59431.3\theta_{\text{neg}}^4 \\ & - 195881.6488\theta_{\text{neg}}^5 + 374577.3152\theta_{\text{neg}}^6 - 385821.1607\theta_{\text{neg}}^7 + 165705.8597\theta_{\text{neg}}^8 \end{aligned} \tag{A.10b}$$

$$\theta_l = \frac{c_{s_l}^*}{c_{\text{s,max}_l}} \qquad l \in \{\text{pos, neg}\} \tag{A.11}$$

$$D_l = 10^{-4}10^{-4.43-\frac{54}{T(t)-229-5\times10^{-3}c_{\text{e}}(x,t)}-0.22\times10^{-3}c_{\text{e}}(x,t)} \qquad l \in \{\text{pos, sep, neg}\} \tag{A.12}$$

$$D_l^{\text{eff}} = D_l\varepsilon_l^{\text{brugg}_l} \qquad l \in \{\text{pos, sep, neg}\} \tag{A.13}$$

$$\begin{aligned} \kappa_l = {} & 10^{-4}c_{\text{e}}(x,t)\left(-10.5 + 0.668\times10^{-3}c_{\text{e}}(x,t) + 0.494\times10^{-6}c_{\text{e}}(x,t)^2 + (0.074 - 1.78\times10^{-5})c_{\text{e}}(x,t) - 8.86\times10^{-10}c_{\text{e}}(x,t)^2\right)T(t) \\ & + \left(-6.96\times10^{-5} + 2.8\times10^{-8}c_{\text{e}}(x,t))T(t)^2\right)^2 \qquad l \in \{\text{pos, sep, neg}\} \end{aligned} \tag{A.14}$$

$$\kappa_{\text{eff}_l} = \kappa_l\varepsilon_l^{\text{brugg}_l} \qquad l \in \{\text{pos, sep, neg}\} \tag{A.15}$$

$$k_{\text{r}_l}^{\text{eff}} = k_{\text{r}_l}e^{\frac{-E_{\text{act,k}_l}}{R}\left(\frac{1}{T(t)}-\frac{1}{T_{\text{sink}}}\right)} \qquad l \in \{\text{pos, neg}\} \tag{A.16}$$

$$D_{\text{s}_l}^{\text{eff}} = D_{\text{s}_l}e^{\frac{-E_{\text{act,s}_l}}{R}\left(\frac{1}{T(t)}-\frac{1}{T_{\text{sink}}}\right)} \qquad l \in \{\text{pos, neg}\} \tag{A.17}$$

$$\sigma_{\text{eff}_l} = \sigma_l\varepsilon_l \qquad l \in \{\text{pos, neg}\} \tag{A.18}$$

Lumped thermal model equations:

$$m_{\text{cell}}c_{\text{avg}}\frac{dT}{dt} = -hA_{\text{tabs}}\left(T(t) - T_{\text{sink}}\right) + Q_{\text{pol}} \tag{A.19}$$

$$Q_{\text{pol}} = A_{\text{cell}}\,|i|\cdot|U - V| \tag{A.19a}$$

$$U = U_{\text{pos}}(\theta_{\text{pos}})\big|_{x=x_{\text{pos/Alcc}}} - U_{\text{neg}}(\theta_{\text{neg}})\big|_{x=x_{\text{neg/Cucc}}} \tag{A.19b}$$

$$V = \phi_{\text{s}}\big|_{x=x_{\text{pos/Alcc}}} - \phi_{\text{s}}\big|_{x=x_{\text{neg/Cucc}}} \tag{A.19c}$$

References

[1] J. B. Goodenough, Electrochemical energy storage in a sustainable modern society, Energy Environ. Sci. 7 (1) (2014) 14–18. doi:10.1039/C3EE42613K.
URL http://xlink.rsc.org/?DOI=C3EE42613K

[2] V. Etacheri, R. Marom, R. Elazari, G. Salitra, D. Aurbach, Challenges in the development of advanced Li-ion batteries: a review, Energy & Environmental Science 4 (9) (2011) 3243. doi:10.1039/c1ee01598b.
URL http://xlink.rsc.org/?DOI=c1ee01598b

[3] B. Scrosati, J. Garche, Lithium batteries: Status, prospects and future, Journal of Power Sources 195 (9) (2010) 2419–2430. doi:10.1016/j.jpowsour.2009.11.048.
URL http://linkinghub.elsevier.com/retrieve/pii/S0378775309020564

[4] N. S. Choi, Z. Chen, S. A. Freunberger, X. Ji, Y. K. Sun, K. Amine, G. Yushin, L. F. Nazar, J. Cho, P. G. Bruce, Challenges facing lithium batteries and electrical double-layer capacitors, Angewandte Chemie - International Edition 51 (40) (2012) 9994–10024. arXiv:9809069v1, doi:10.1002/anie.201201429.
URL http://doi.wiley.com/10.1002/anie.201201429

[5] A. Vlad, N. Singh, C. Galande, P. M. Ajayan, Design Considerations for Unconventional Electrochemical Energy Storage Architectures, Advanced Energy Materials 5 (19) (2015) 1402115. doi:10.1002/aenm.201402115.
URL http://doi.wiley.com/10.1002/aenm.201402115

[6] S. Arora, W. Shen, A. Kapoor, Review of mechanical design and strategic placement technique of a robust battery pack for electric vehicles, Renewable and Sustainable Energy Reviews 60 (2016) 1319–1331. doi:10.1016/j.rser.2016.03.013.
URL http://linkinghub.elsevier.com/retrieve/pii/S1364032116002483

[7] I. A. Hunt, Y. Zhao, Y. Patel, J. Offer, Surface Cooling Causes Accelerated Degradation Compared to Tab Cooling for Lithium-Ion Pouch Cells, Journal of The Electrochemical Society 163 (9) (2016) A1846–A1852. doi:10.1149/2.0361609jes.
URL http://jes.ecsdl.org/lookup/doi/10.1149/2.0361609jes

[8] L. Lu, X. Han, J. Li, J. Hua, M. Ouyang, A review on the key issues for lithium-ion battery management in electric vehicles, Journal of Power Sources 226 (2013) 272–288. doi:10.1016/j.jpowsour.2012.10.060.
URL http://dx.doi.org/10.1016/j.jpowsour.2012.10.060

[9] S. H. Thomke, Simulation, learning and R&D performance: Evidence from automotive development, Research Policy 27 (1) (1998) 55–74. doi:10.1016/S0048-7333(98)00024-9.
URL http://linkinghub.elsevier.com/retrieve/pii/S0048733398000249

[10] M. C. Becker, P. Salvatore, F. Zirpoli, The impact of virtual simulation tools on problem-solving and new product development organization, Research Policy 34 (9) (2005) 1305–1321. doi:10.1016/j.respol.2005.03.016.
URL http://linkinghub.elsevier.com/retrieve/pii/S0048733305001307

[11] R. M. Spotnitz, Battery modeling, The Electrochemical Society Interface (2005) 39 – 42doi:10.1109/MC.2003.1250886.

[12] A. Jokar, B. Rajabloo, M. Désilets, M. Lacroix, Review of simplified Pseudo-two-Dimensional models of lithium-ion batteries, Journal of Power Sources 327 (2016) 44–55. doi:http://dx.doi.org/10.1016/j.jpowsour.2016.07.036.
URL http://www.sciencedirect.com/science/article/pii/S0378775316308916

[13] S. Nejad, D. Gladwin, D. Stone, A systematic review of lumped-parameter equivalent circuit models for real-time estimation of lithium-ion battery states, Journal of Power Sources 316 (2016) 183–196. doi:10.1016/j.jpowsour.2016.03.042.
URL http://linkinghub.elsevier.com/retrieve/pii/S0378775316302427

[14] M. S. Islam, C. A. J. Fisher, Lithium and sodium battery cathode materials: computational insights into voltage, diffusion and nanostructural properties, Chem. Soc. Rev. 43 (1) (2014) 185–204. doi:10.1039/C3CS60199D.
URL http://xlink.rsc.org/?DOI=C3CS60199D

[15] Y. S. Meng, M. E. Arroyo-de Dompablo, First principles computational materials design for energy storage materials in lithium ion batteries, Energy & Environmental Science 2 (6) (2009) 589. doi:10.1039/b901825e.
URL http://xlink.rsc.org/?DOI=b901825e

[16] A. D. Sendek, Q. Yang, E. D. Cubuk, K.-A. N. Duerloo, Y. Cui, E. J. Reed, Holistic computational structure screening of more than 12 000 candidates for solid lithium-ion conductor materials, Energy Environ. Sci. 10 (1) (2017) 306–320. doi:10.1039/C6EE02697D.
URL http://xlink.rsc.org/?DOI=C6EE02697D

[17] V. Ramadesigan, P. W. C. Northrop, S. De, S. Santhanagopalan, R. D. Braatz, V. R. Subramanian, Modeling and Simulation of Lithium-Ion Batteries from a Systems Engineering Perspective, Journal of the Electrochemical Society 159 (3) (2012) R31–R45. doi:10.1149/2.018203jes.
URL http://jes.ecsdl.org/cgi/doi/10.1149/2.018203jes

[18] M. Doyle, T. F. Fuller, J. Newman, Modeling of Galvanostatic Charge and Discharge of the Lithium/Polymer/Insertion Cell, Journal of The Electrochemical Society 140 (6) (1993) 1526–1533. doi:10.1149/1.2221597.
URL http://link.aip.org/link/?JES/140/1526/1

[19] L. Cai, R. E. White, Mathematical modeling of a lithium ion battery with thermal effects in COMSOL Inc. Multiphysics (MP) software, Journal of Power Sources 196 (14) (2011) 5985–5989. doi:10.1016/j.jpowsour.2011.03.017.
URL http://linkinghub.elsevier.com/retrieve/pii/S0378775311005994

[20] A. Jarrett, I. Yong Kim, Design Optimization of Electric Vehicle Battery Cooling Plates for Thermal Performance, Journal of Power Sources (2010). doi:10.1016/j.jpowsour.2011.06.090.
URL http://linkinghub.elsevier.com/retrieve/pii/S0378775311013279

[21] N. Legrand, B. Knosp, P. Desprez, F. Lapicque, S. Raël, Physical characterization of the charging process of a Li-ion battery and prediction of Li plating by electrochemical modelling, Journal of Power Sources 245 (2014) 208–216. doi:10.1016/j.jpowsour.2013.06.130.
URL http://linkinghub.elsevier.com/retrieve/pii/S0378775313011373

[22] P. Albertus, J. Newman, FORTRAN Programs for the Simulation of Electrochemical Systems (2007).
URL http://www.cchem.berkeley.edu/jsngrp/fortran.html

[23] M. Torchio, L. Magni, R. B. Gopaluni, R. D. Braatz, D. M. Raimondo, LIONSIMBA: A Matlab Framework Based on a Finite Volume Model Suitable for Li-Ion Battery Design, Simulation, and Control, Journal of The Electrochemical Society 163 (7) (2016) A1192–A1205. doi:10.1149/2.0291607jes.
URL http://jes.ecsdl.org/lookup/doi/10.1149/2.0291607jes

[24] J. Newman, Optimization of Porosity and Thickness of a Battery Electrode by Means of a Reaction-Zone Model, Journal of The Electrochemical Society 142 (1) (1995) 97. doi:10.1149/1.2043956.
URL http://jes.ecsdl.org/cgi/doi/10.1149/1.2043956

[25] C. R. Pals, J. Newman, Thermal Modeling of the Lithium/Polymer Battery, Journal of The Electrochemical Society 142 (10) (1995) 3282. doi:10.1149/1.2049975.
URL http://jes.ecsdl.org/cgi/doi/10.1149/1.2049975

[26] P. W. C. Northrop, V. Ramadesigan, S. De, V. R. Subramanian, Coordinate Transformation , Orthogonal Collocation , Model Reformulation and Simulation of Electrochemical-Thermal Behavior of Lithium-Ion Battery Stacks, Journal of The Electrochemical Society 158 (12) (2011) A1461–A1477. doi:10.1149/2.058112jes.

[27] J. Newman, K. E. Thomas-Alyea, Electrochemical Systems, 3rd Edition, John Wiley & Sons, Hoboken, 204. arXiv:arXiv:1011.1669v3, doi:10.1017/CBO9781107415324.004.

[28] S. Golmon, K. Maute, M. L. Dunne, Multiscale design optimization of lithium-ion batteries using adjoint sensitivity analysis, International Journal For Numerical Methods in Engineering 92 (2012) 474–494. arXiv:1010.1724, doi:10.1002/nme.

[29] S. Y. Choe, X. Li, M. Xiao, Fast charging method based on estimation of ion concentrations using a reduced order of electrochemical thermal model for lithium ion polymer battery, World Electric Vehicle Journal 6 (3) (2013) 782–792. doi:10.1109/EVS.2013.6914966.

[30] Matlab, The mathworks, Inc., Natick, MA 2017a (2017) –.

[31] R. Yazami, Y. Ozawa, H. Gabrisch, B. Fultz, New Trends in Intercalation Compounds for Energy Storage Conversion, The Electrochemical Society, Pennington, 2003.

[32] SAE Hybrid Committee, SAE Charging Configurations and Ratings Terminology (2011).
URL http://www.sae.org/smartgrid/chargingspeeds.pdf

[33] R. Kizilel, R. Sabbah, J. R. Selman, S. Al-Hallaj, An alternative cooling system to enhance the safety of Li-ion battery packs, Journal of Power Sources 194 (2) (2009) 1105–1112. doi:10.1016/j.jpowsour.2009.06.074.
URL http://linkinghub.elsevier.com/retrieve/pii/S0378775309011458

[34] General Motors, Drive Unit and Battery at the Heart of Chevrolet Bolt EV (2016).
URL http://www.gm.com/mol/m-2016-Jan-naias-chevy-0111-bolt-du.html

[35] O. Gröger, H. a. Gasteiger, J.-P. Suchsland, Review—Electromobility: Batteries or Fuel Cells?, Journal of The Electrochemical Society 162 (14) (2015) A2605–A2622. doi:10.1149/2.0211514jes.
URL http://jes.ecsdl.org/lookup/doi/10.1149/2.0211514jes

[36] P. Svens, M. H. Kjell, C. Tengstedt, G. Flodberg, G. Lindbergh, Li-ion pouch cells for vehicle applications-studies of water transmission and packing materials, Energies 6 (2013) 400–410. doi:10.3390/en6010400.

[37] S. C. Chen, C. C. Wan, Y. Y. Wang, Thermal analysis of lithium-ion batteries, Journal of Power Sources 140 (1) (2005) 111–124. doi:DOI: 10.1016/j.jpowsour.2004.05.064.
URL http://www.sciencedirect.com/science/article/B6TH1-4DF49BM-2/2/a6c383e4ffa32dba3641a1e863344ae9

[38] G. Guo, B. Long, B. Cheng, S. Zhou, P. Xu, B. Cao, Three-dimensional thermal finite element modeling of lithium-ion battery in thermal abuse application, Journal of Power Sources 195 (8) (2010) 2393–2398. doi:DOI: 10.1016/j.jpowsour.2009.10.090.
URL http://www.sciencedirect.com/science/article/B6TH1-4XMD5JV-8/2/f21e0783e039fc823be5b61bfb87d645

[39] W. Martienssen, H. Warlimont, Springer Handbook of Condensed Matter and Materials Data, Springer Berlin Heidelberg, Berlin, 2005. arXiv:arXiv:1011.1669v3, doi:10.1007/3-540-30437-1.
URL http://www.springerlink.com/index/10.1007/3-540-30437-1{%}5Cnhttp://link.springer.com/10.1007/3-540-30437-1

[40] D. H. Jeon, S. M. Baek, Thermal modeling of cylindrical lithium ion battery during discharge cycle, Energy Conversion and Management 52 (8-9) (2011) 2973–2981. doi:10.1016/j.enconman.2011.04.013.
URL http://dx.doi.org/10.1016/j.enconman.2011.04.013

[41] C. F. Lopez, J. A. Jeevarajan, P. P. Mukherjee, Characterization of Lithium-Ion Battery Thermal Abuse Behavior Using Experimental and Computational Analysis, Journal of The Electrochemical Society 162 (10) (2015) A2163–A2173. doi:10.1149/2.0751510jes.
URL http://jes.ecsdl.org/lookup/doi/10.1149/2.0751510jes

[42] U. S. Kim, C. B. Shin, C. S. Kim, Modeling for the scale-up of a lithium-ion polymer battery, Journal of Power Sources 189 (1) (2009) 841–846. doi:10.1016/j.jpowsour.2008.10.019.

[43] V. R. Subramanian, V. Boovaragavan, V. Ramadesigan, M. Arabandi, Mathematical Model Reformulation for Lithium-Ion Battery Simulations : Galvanostatic Boundary Conditions, Journal of the Electrochemical Society 156 (4) (2009) A260–A271. doi:10.1149/1.3065083.

[44] G. L. Plett, Battery Management Systems, Volume II: Equivalent-Circuit Methods, Artech House, Norwood, Massachusetts, 2016.

[45] D. W. Dees, V. S. Battaglia, A. Belanger, Electrochemical modeling of lithium polymer batteries, Journal of Power Sources 110 (2) (2002) 310–320. doi:DOI: 10.1016/S0378-7753(02)00193-3.
URL http://www.sciencedirect.com/science/article/B6TH1-45TTRFJ-1/2/694510c6a30d57990eadcc4bd70389e6

[46] A. C. Hindmarsh, P. N. Brown, K. E. Grant, S. L. Lee, R. Serban, D. E. Shumaker, C. S. Woodward, SUNDIALS: Suite of nonlinear and differential/algebraic equation solvers, ACM Transactions on Mathematical Software (TOMS) 31 (3) (2005) 363—-396.

[47] S. Santhanagopalan, R. E. White, Online estimation of the state of charge of a lithium ion cell, Journal of Power Sources 161 (2) (2006) 1346–1355. doi:10.1016/j.jpowsour.2006.04.146.
URL http://linkinghub.elsevier.com/retrieve/pii/S0378775306008068

[48] S. Santhanagopalan, Q. Guo, P. Ramadass, R. E. White, Review of models for predicting the cycling performance of lithium ion batteries, Journal of Power Sources 156 (2) (2006) 620–628. doi:DOI: 10.1016/j.jpowsour.2005.05.070.
URL http://www.sciencedirect.com/science/article/B6TH1-4GM4620-7/2/022854c2137ca57cdc1f45fb0d5542e2

[49] L. N. Trefethen, Spectral Methods in MATLAB, Society for Industrial and Applied Mathematics, 2000.

[50] A. M. Bizeray, S. Zhao, S. R. Duncan, D. a. Howey, Lithium-ion battery thermal-electrochemical model-based state estimation using orthogonal collocation and a modified extended Kalman filter, Journal of Power Sources (2015) 400–412doi:10.1016/j.jpowsour.2015.07.019.

[51] J. Andersson, Faculty of Engineering Science A General-Purpose Software Framework for Dynamic Optimization, Ph.D. thesis, Arenberg Doctoral School, KU Leuven (2013).

[52] M. Yilmaz, P. T. Krein, Review of charging power levels and infrastructure for plug-in electric and hybrid vehicles, 2012 IEEE International Electric Vehicle Conference, IEVC 2012 28 (5) (2012) 2151–2169. doi:10.1109/IEVC.2012.6183208.

[53] R. H. Ashique, Z. Salam, M. J. Bin Abdul Aziz, A. R. Bhatti, Integrated photovoltaic-grid dc fast charging system for electric vehicle: A review of the architecture and control, Renewable and Sustainable Energy Reviews 69 (May 2016) (2017) 1243–1257. doi:10.1016/j.rser.2016.11.245.
URL http://dx.doi.org/10.1016/j.rser.2016.11.245

[54] S. Srdic, C. Zhang, X. Liang, W. Yu, S. Lukic, A SiC-based Power Converter Module for Medium- Voltage Fast Charger for Plug-in Electric Vehicles, Proc. IEEE Appl. Power Electron. Conf. and Expo. (APEC) (2016) 2714–2719doi:10.1109/APEC.2016.7468247.

[55] N. Jeff, 2017 Chevy Bolt EV Is Less of a Drag Than Originally Believed (2017).
URL http://www.hybridcars.com/2017-chevy-bolt-ev-is-less-of-a-drag-than-originally-believed/

[56] Chevrolet Bolt Features - Dimensions.
URL http://www.chevrolet.com/byo-vc/client/en/US/chevrolet/bolt-ev/2017/bolt-ev/features/trims/?section=Highlights{&}section=Exterior{&}section=Dimensions{&}styleOne=388584

[57] Society of Automotive Engineers, SAE Standard J1666 "Hybrid Electric Vehicle Acceleration, Gradeability, and Deceleration Test Procedure", Tech. rep., Society of Automotive Engineers (2004).

[58] Chevrolet Bolt - Overview.
URL http://www.chevrolet.com/bolt-ev-electric-vehicle-2

[59] J. Liu, M. Anwar, P. Chiang, S. Hawkins, Y. Jeong, F. Momen, S. Poulos, S. Song, Design of the Chevrolet Bolt EV Propulsion System, SAE International Journal of Alternative Powertrains 5 (1) (2016) 2016–01–1153. doi:10.4271/2016-01-1153.
URL http://papers.sae.org/2016-01-1153/

[60] M. Ehsani, Y. Gao, A. Emadi, Modern Electric , Hybrid Electric , and Fuel Cell Vehicles. Fundamentals, Theory and Design, 2nd Edition, CRC Press. Taylor & Francis Group, Boca Raton, 2010.

[61] Chevrolet Bolt EV Specifications.
URL http://media.chevrolet.com/media/us/en/chevrolet/vehicles/bolt-ev/2017.tab1.html

[62] F. Markus, General Motors Details New Modular I-3, I-4 Engines (2014).
URL http://www.motortrend.com/news/gm-introduces-extra-small-block-ecotec-engine-family/